NZP-type ceramics for simultaneous incorporation of radioisotopes of cesium strontium and minor actinides

by

L.M. van Koppen

in partial fulfilment of the requirements for the degree of

Bachelor of Science
in Molecular Science and Technology

at the Delft University of Technology
Faculty of Applied Sciences
Department of Radiation Science and Technology
Section of Nuclear Energy and Radiation Applications

Student number:	4226917
Email:	lmvankoppen@student.tudelft.nl
Supervisors:	Dr. Denis Bykov
	Prof. Dr. Ir. Jan Leen Kloosterman

TU Delft Delft University of Technology

Abstract

With the possible upscaling of nuclear energy into a sustainable society, the treatment of radioactive waste is a growing concern. The immobilization of waste into a matrix is a possibility for safe storage. NZP type ceramics are promising materials for this immobilization of radioactive waste. In this thesis the characterization and phase analysis of these NZP type phosphates containing fission products cesium and strontium was done, and subsequently the synthesis of these ceramics containing cerium as a model for radioactive actinides was studied. To this end three series of cesium and strontium containing NZP type ceramics were synthesized using the mechanochemical method of synthesis and characterized via X-ray diffraction and IR spectroscopy. Further characterization on samples representing the cesium and strontium waste stream were done by leaching testing, differential thermal analysis and thermogravimetric analysis. Cerium containing NZP type ceramics were attempted to be synthesised using a similar mechanochemical method. In the series of cesium and strontium containing NZP type ceramics we saw the formation of two individual NZP phases, one Cs and one Sr-rich, except for the series of $Sr_{1-(x/2)}[Zr_{1+x}Fe_{1-x}(PO_4)_3]$ which formed a solid solution. IR spectra proved the presence of orthophopshates and the space groups of the end members $Cs[Zr_2(PO_4)_3]$ and $Sr_{0.5}[Zr_2(PO_4)_3]$ of $R\bar{3}c$ and $R\bar{3}$ respetively while leaving the structure of $Sr[ZrFe(PO_4)_3]$ unclear. Leaching rates for strontium in NZP phases were found to be 131 $\frac{\mathrm{mg}}{\mathrm{m^2 day}}$ and 12.4 $\frac{\mathrm{mg}}{\mathrm{mg^2 day}}$ for $Cs_{0.6}Sr_{0.4}[Zr_{1.6}Fe_{0.4}(PO_4)_3]$ and $Cs_{0.4}Sr_{0.3}[Zr_2(PO_4)_3]$ respectively after Soxhlet leaching of 21 days. Temperatures of crystallization and decomposition were found to be approximately 600 and 1300 °C respectively. Lastly the formation of tetravalent cerium in NZP was successful albeit with low crystallinity whilst the synthesis of trivalent cerium in NZP was not successful.

Contents

1

Introduction

We live in a society where electricity seems a given fact, we would be completely lost without it. It's therefore strange to imagine that one day our fossil fuels will run out leading to a massive shortage of power for everyone. To make sure this doesn't happen we need other energy sources, the advancements in solar cells, windmills and other durable energy are still too little to make up for our fossil fuel demand. To span this gap from our fossil fuel economy to a durable society we need nuclear energy. Nuclear energy has been put in a bad daylight by events such as Chernobyl and Fukushima, yet it isn't as dangerous as everyone makes it out to be as shown by the world nuclear association [1]. Nuclear waste requires a reliable means of immobilization and if the world's nuclear energy production is going to be increased advancements in this field need to be made. As of now approximately 10,000 m^3 of high-level waste (HLW) is produced every year [2]. This HLW makes up for 95 % of all radio-toxicity that is generated through nuclear energy and consists of long lived actinides and shorter lived fission products.

1.1. High Level Waste

High level nuclear waste consists of fission products and various actinides. And whilst the quantity is rather low the radio-toxicity is high and lasts long as can be seen in figure 1.1.

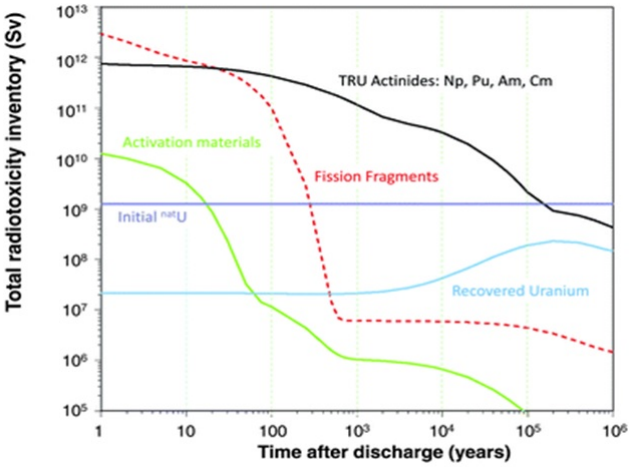

Figure 1.1: The radio toxicity of the high level waste products against the time after discharge.[3]

In this figure we see that the fission products are relatively short lived at 300 years compared to the actinides which take about 10.000 years to decay to a tolerable level. Therefore there would be much to gain by immobilizing these products separately until they are decayed to safe level.

1.1.1. Fission products cesium and strontium

Of all fission products Cs-137 and Sr-90 are the biggest heat emitters present in HLW with respective specific power of 0.097 W.g^{-1} and 0.142 W.g^{-1} [4]. The half lives of these isotopes are rather similar 30 years for Cs-137 and 28.8 years for Sr-90. If these two isotopes can be packed simultaneously into a stable waste form this would reduce the volume of radioactive waste by removing these high heat emitting isotopes more radioactive waste can be immobilised at once without reaching too high temperatures in the repository. This however would require simultaneous extraction of these two isotopes, luckily various schemes have been developed and demonstrated to do just that [4]. These processes have even proven to be extremely efficient and result in a process stream of 59.2 mole% caesium and 40.8 mole% strontium [4].

1.1.2. Actinides

As seen in figure 1.1 actinides have a high radio-toxicity for approximately 10.000 years. This long decay period is a result of the nuclear chain decay an example of such a chain is shown in figure 1.2.

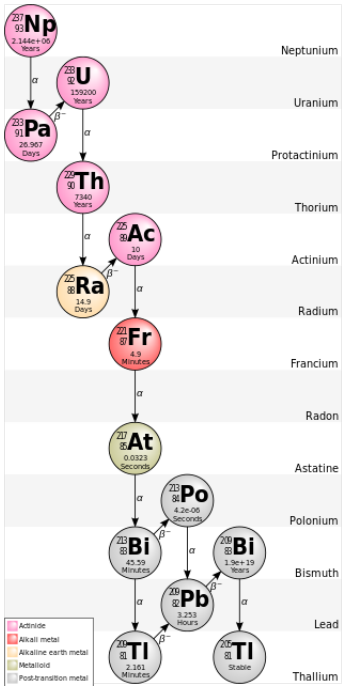

Figure 1.2: Decay chain of the Neptunium series, shown are the decay product with their half lives

The actinides show a wide variety in chemical behaviour and oxidation states, however most actinides are either tri- or tetravalent. To avoid working with highly radioactive isotopes of these elements we can use their non-radioactive chemical analogues. This can be achieved by using lanthanides such as cerium.

1.2. Ceramic waste forms

The current technology for immobilisation of HLW is solidifcation of the entire content into a glass matrix, the most often used glass is borosilicate glass which is mainly used in France and the UK [5]. These glasses however have some disadvantages in the form of devitrification, the crystallization of amorphous glass which happens in the presence of water, and also thermodynamic instability as demonstrated by Montel et al. [6]. Ceramic materials based on natural minerals draw attention due to their desireable properties with regard to chemical, thermal and even radiation stability [6]. There are various possible ceramic waste forms based on a wide variety of natural minerals as shown in table 1.1 this is a table of some ceramic materials which can be used as waste forms [7].

Table 1.1: Table showing various different ceramic materials and the radionuclides they could capture [7].

Phase	Radionuclide
Pollucite, $CsAlSi_2O_6$	Cs
Hollandite, $(Cs,Sr,Ba,Rb)_{1.14}(Al,Ti^{3+},Fe)_{2.28}TiO_{16}$	Cs, Rb, Sr, Ba
Feldspar, $CaAl_2Si_2O_8$	Sr,Ba
Apatite, $Ca_{10}([P,Si]O_4)_6(OH,F,Cl)_2$	RE, An, Sr, Ba
NZP, $(Na,Ca_{0.5}(Zr,Ti)_2(PO_4)_3$	Many
Monazite, $REPO_4$	RE,An
Garnet, $Ca_{1.5}GdTh_{0.5}FeFe_3SiO_{12}$	RE, An
Zircon, $ZrSiO_4$	RE, An
Xenotime, YPO_4	RE, An
Zirconolite, $CaZrTi_2O_7$	RE, An
Perovskite, $CaTiO_3$	Sr, RE, Tc, An
Fluorite, $(RE,An)O_2$	RE, An
Pyrochlore, $RE_2Ti_2O_7$	RE, Zr, An
Titanite, $CaTiSiO_5$	RE, An, Sr
Rutile, TiO_2	Tc
Sodalite, $Na_4Al_3Si_3O_{12}I$	I
RE: Rare Earth, An: Actinide, NZP: sodium zirconium phosphate	

Many of these ceramics have been extensively studied for the possible immobilisation of various radioactive isotopes. For example cesium has been found to be quite stable in the pollucite structure whilst strontium has been studied in the feldspar type [8]. However these structure types do not allow for co-packing of these two elements. That is why in this thesis we will focus on the structure type of $NaZr_2(PO_4)_3$ abbreviated as NZP, because it can contain a lot of different radioactive isotopes, and furthermore shows promising properties [9]. Subsequently, phosphate groups are present in the waste stream as a result of UREX extraction in the form of tri-butyl phosphate and zirconium is also found in this stream as it is used in various parts of a reactor giving us the possibility to leave no waste unused.

1.2.1. NZP type ceramics

NZP type ceramics are based on the natural minerals kosnarite, $KZr_2(PO_4)_3$, the simplest NZP is also its synthetic analogue sodium zirconium phosphate or $Na[Zr_2(PO_4)_3]$.

The NZP structure was first determined by Hagman et al. [10].They found that NZP crystallizes in a trigonal crystal system, with lattice hexagonal and space group $R\bar{3}c$. A hexagonal unit cell is shown in figure 1.3, this particular lattice has sides a=b≠c and angles α=β=90°, γ=120°.

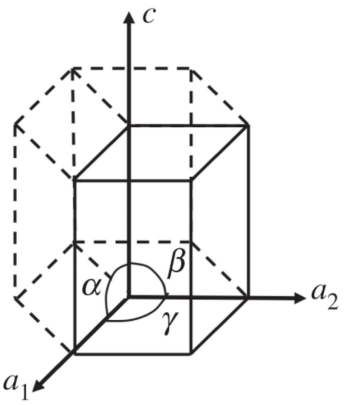

Figure 1.3: A hexagonal unit cell.

Each zirconium forms a ZrO_6 octahedron, which is surrounded by six PO_4 tetrahedra which are surrounded by four ZrO_6 octahedra by sharing the terminal oxygen. These polyhedra form the framework

of the unit cell. The crystal chemical formula for the NZP type structure is (M1)(M2)[$L_2(PO_4)_3$], here M1 and M2 are void cations that fill the cavities in the framework, whilst L cations fill the framework. In the case of sodium zirconium phosphate only the M1 cavities are filled. We find these cavities between two framework octahedra, causing the sodium to form an antiprism by sharing six oxygen atoms with these framework octahedra [11]. This structure is shown in figure 1.4.

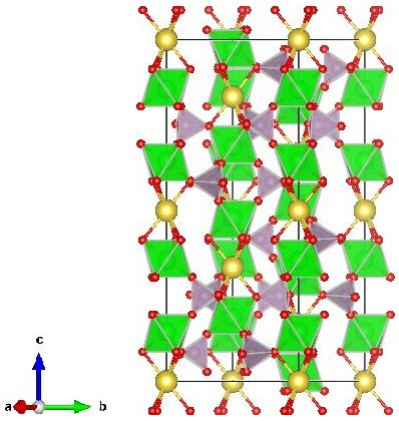

Figure 1.4: The NZP unit cell, here sodium is represented as yellow, zirconium as green, phosphorus as purple and oxygen as red. Where applicable the polyhedra are shown. This figure was produced using Vesta [12]

Isomorphism

The NZP structure type has been found to be able to accommodate a wide variety of cations in its structure [13]. These cations can fill the two void slots as mentioned before. The M1 position can for example hold small cations such as lithium and sodium but also much bigger cations as cesium and strontium. The M2 positions is more limited in this respect as it can only hold small cations such as lithium and sodium. In the framework of the structure, the L position, small cations can be held but also actinides such as uranium and plutonium as will be shown later.

This high isomorphic capacity is a great feature for immobilizing radioactive waste because it means we can synthesize various NZP type phosphates with different cation stoichiometry. As shown by Hawkins et al. [14] uranium can be accommodated in the framework cation position L in the form of $KZr_{2-x}U_x(PO_4)_3$. As shown by Bohre and Shrivastava, cesium and strontium can be loaded simultaneously unto the NZP structure [15] as $Na_{1-x}(Cs_{1.33}Sr)_xZr_2(PO_4)_3$. The packing of trivalent lanthanides, as $La_{0.33}Zr_2(PO_4)_3$, has also been studied by Bykov et al. [16]. Only little research was done on the possible accommodation of tri- and tetravalent actinides into the M1 position.

Thermal properties

Due to its wide variety of possible applications there has been extensive research done into the properties of the NZP structure type [17]. Good thermal properties are desirable for immobilizing radioactive waste as the structure needs to withstand the heat from both the repository and more importantly the emitted heat from the radioactive isotopes.

Sodium zirconium phosphate was found to have a thermal expansion coefficient of only 10^{-6} °C^{-1} [18] which is comparable to the presently used borosilicate glass [19] meaning the ceramic could safely be stored without fear of cracking due to the cell's expansion. Additionally temperature of decomposition was found to be as high as 1700 °C for sodium zirconium phosphate, when the chemical formula is changed the decomposition temperatures tend to decrease for example $Sr_{0.5}[Zr_2(PO_4)_3]$ was found to have a decomposition temperature of 1650 °C.

Leaching rates

Leachability of cesium and strontium containing NZP compounds have also been studied. The leaching rate of $Cs[Zr_2(PO_4)_3]$ for example was measured to be 0.04 $\frac{mg}{m^2 day}$ in deionised water after 7 days of leaching at 90 °C [20]. Additionally the leaching rate of $Sr[ZrFe(PO_4)_3]$ was found to be 0.22 $\frac{mg}{m^2 day}$ in deionised water after 16 days at 90 °C [21]. Both these rates out perform other structure types such as hollandite which were 3 and 4 $\frac{mg}{m^2 day}$ for Cs and Sr respectively [22].

Solid solutions

In the work of Bohre et al [15] the series of $Na_{1-x}(Cs_{1.33}Sr)_xZr_2(PO_4)_3$ was studied, this solid solution was synthesized via the conventional solid state reaction method. They found that for weight percentages below approximately 14.46 and 7.16 for cesium and strontium respectively phase pure NZP was synthesized but for higher percentages traces of a secondary phase of cesium strontium zirconium phosphate started to form along with the solid solution. Through analytical evidence they were able to determine that cesium and strontium were crystallochemically fixed in the ceramic matrix.
Naik et al. [20] synthesized a NZP phase with small percentages of cesium and strontium, both 1% into the matrix. For this purpose they used low temperature microwave assisted synthesis. They found very low leaching values and that doping the matrix with additional cesium and strontium would reduce leaching even further.
In the bachelor's thesis of Priya Jagai [23] the formation of a solid solution in the series of $Cs_xSr_{1-(x/2)}[Zr_{1+x}Fe_{1-x}(PO_4)_3]$ with the additional formation of addmixtures in the form of zirconium pyrophosphate and iron oxide was reported. This solid solution was synthesized via the mechanochemical synthesis route. As this synthesis method was found to produce the most crystalline samples this method will also be used in the present work. Not much characterization was done on these samples but the author found a low leaching rate for one of the end members.

1.3. Goal

The goal of this thesis is twofold. Firstly we want to synthesize a NZP-type ceramic that contains both cesium and strontium using the mechanochemical synthesis method, even though Goldschmidt's rule states the difference between ions can not exceed 15%, which is the case for Cs and Sr, there have already been many exceptions to this empirical rule [24]. Furthermore we want to characterize these NZP structures via X-ray diffraction, phase formation studies, leaching tests, DTA/TG and IR-spectroscopy.
Secondly we want to optimise the possible synthesis of NZP type ceramics containing minor actinides by using the inactive analogue cerium as a model.

2

Experimental

2.1. Synthesis of NZP-type ceramics

2.1.1. Cesium and Strontium containing NZP-type ceramics

In order to obtain a solid solution of NZP-type ceramics containing both cesium and strontium, we investigated three different compositions as shown in figure 2.1. The end members of these compositions are known to crystallize in an NZP-type.

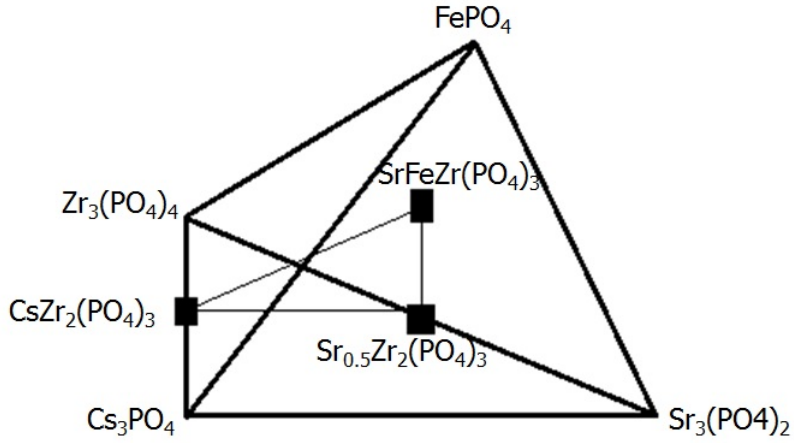

Figure 2.1: A representation of the three different NZP compositions that contain cesium and/or strontium

These three compositions can be represented as followed:

1. $Cs_xSr_{(1-x)/2}[Zr_2(PO_4)_3]$
2. $Sr_{1-(x/2)}[Zr_{1+x}Fe_{1-x}(PO_4)_3]$
3. $Cs_xSr_{1-(x/2)}[Zr_{1+x}Fe_{1-x}(PO_4)_3]$

(With x=0, 0.2, 0.4, 0.6, 0.8 and 1.) As shown by Jagai [23] the preferred synthesis method of these compounds is mechanochemical synthesis. This particular synthesis method is shown in figure 2.2

Mechanochemical synthesis

This synthesis method uses ball milling as a means of homogenization and synthesizing an amorphous product as was shown by Rojac and Kosac [25]. Ball milling employs balls inside the jars, loaded with powder, which are placed into a rotary mill. As a result of the rotation, the balls will grind the powder with high energy resulting in mixing and possible synthesis of intermediate products.

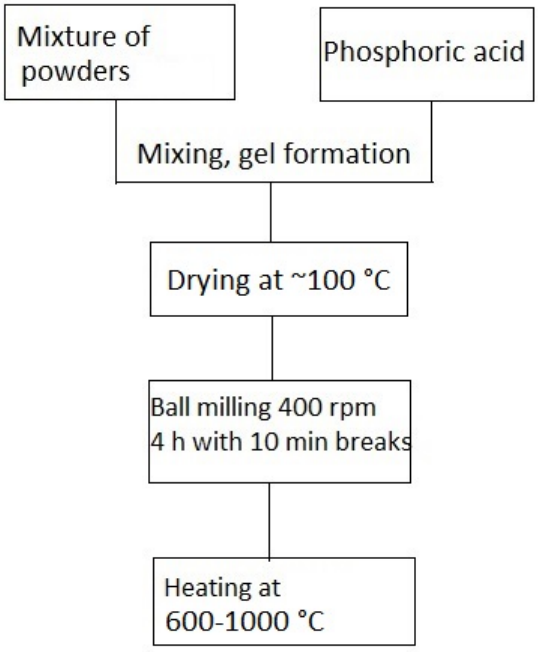

Figure 2.2: Schematic representation of the mechanochemical synthesis method.

Important parameters for this synthesis are the RPM and length of ball milling, the temperature of crystallization and stoichiometry of the initial powders. In this thesis the planetary ball mill of Retch PM400 was used, with jars and balls made of tungsten carbide. A rotational speed of 400 RPM was chosen and a length of milling of 4 hours, this is including ten minute breaks in a ten minute interval. Temperatures of subsequent heat treatments were varied between 600 and a 1000 °C, or combination of multiple heating steps within this range. Most samples were first heated at 600 followed by crystallization at 1000 °C, but this last temperature was also lowered to 800 °C or 850 °C for some of the samples.

Pechini method

Another synthesis method was applied, namely the Pechini method. This method involves polyesterification using citric acid and ethylene glycol, as shown in figure 2.3. For a high temperature synthesis that is diffusion limited using this method should increase efficiency as it immobilizes the cations during gell formation leading to a homogeneous mixture at high temperatures increasing the chances of reaction.

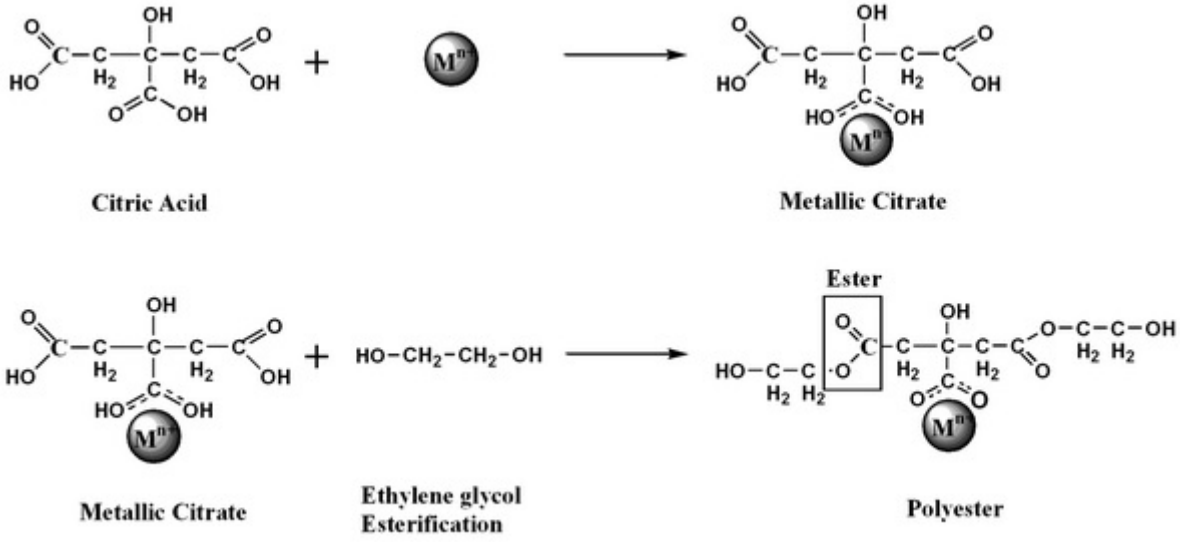

Figure 2.3: Chemical representation of the organic chemistry in the pechini method of synthesis. A metal cation is immobilized by one of the acid groups of citric acid which subsequently forms a polyester with ethylene glycol with the remaining two acid groups [26].

This method has also been proven to work for the synthesis of NZP-type ceramics with the composition $La_{1/3}Zr_2(PO_4)_3$ by Barre et al. [27], following the synthesis route schematically represented in figure 2.4.

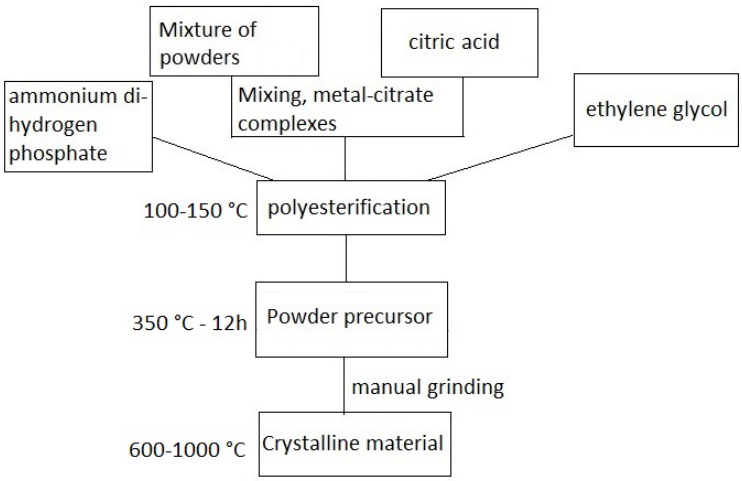

Figure 2.4: Schematic representation of the full synthesis route to form NZP-type ceramics using the Pechini method based on the work of Barre et al. [27]

2.1.2. Cerium containing NZP-type ceramics

Cerium exhibits two oxidation states, +3 and +4. Both of these can be used to model radioactive actinides because especially the highly radiotoxic minor actinides take either of these oxidation states. Whilst cerium oxide allows for stable tetravalent cerium, in solution it would reduce to its trivalent state similar to americium oxide. Due to this additional hurdle an alternative synthesis route was taken as shown in figure 2.5. In an attempt to obtain trivalent cerium in our NZP-type ceramic we performed crystallization in an argon atmosphere as Bregiroux et al. [28] showed that plutonium reduced in this atmosphere by the presence of phosphate.

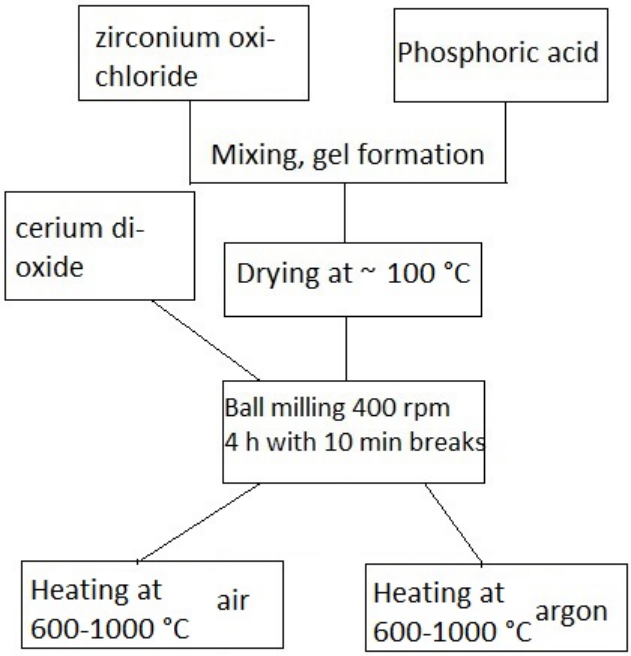

Figure 2.5: Schematic representation of the synthesis route used to obtain cerium containing NZP-type ceramics. Crystallization was done in air for a tetravalent products whilst argon was used for trivalent.

2.2. Characterization of NZP-type ceramics

2.2.1. X-ray Diffraction

For characterization of the powders X-ray Diffraction was used. This particular measuring technique is based on Bragg's law which is shown in equation 2.1, this law expresses the diffraction angles of a specific crystal.

$$n\lambda = 2dsin(\theta) \tag{2.1}$$

In this equation n is an integer 1,2,3..., λ is the wavelength of the X-rays in nm, d constitutes the interplanar distance between lattice planes in nm whilst θ is the incident angle. This equation shows the conditions under which constructive interference occurs resulting in a highly intense bragg peak of diffraction. These bragg peaks are characteristic to a lattice which makes it possible to determine present phases but also cell parameters [29] using programs which will be explained further on. XRD measurements were done at 45 kV, 40 mA in the 2θ range of 5-80° using the instrument X'pert Pro MPD DY2977. The 2θ range of measurement is the array of angles the instrument checks for diffraction.

Phase Analysis

To determine what crystalline phases were measured and thus present in our samples a phase analysis must be performed. This means that we look to cover all experimental diffractions with theoretical ones to see if they are indeed present. For this purpose Powdercell 2.2 [30] and Highscore suite [31] were used. Powdercell plots theoretical diffractograms based on crystallographic data obtained from in this work Pearson's Crystal Data [32]. Highscore does not require the input of crystallographic data as it uses a database of theoretical diffraction patterns.

Rietveld Refinement

The X-ray diffraction pattern gives an indication towards the cell parameters of the lattice. To determine these parameters refinement procedures are useful, for this purpose Hugo Rietveld proposed a profile refinement [33] which would come to carry his name. This refinement has become a go-to method in the crystallographic field due to its reliable results. Rietveld refinement uses a least squares approach to refine the theoretical profile to the experimental as shown by equation 2.2.

$$M = \sum_i W_i (y_i^{obs} - \frac{1}{c} y_i^{calc}) \tag{2.2}$$

The purpose of the refinement is to minimize function M which analyses the difference between a calculated theoretical profile y^{calc} and the observed experimental one y^{obs}, in this equation W_i is the statistical weight of point i whereas c is an overall scale factor. This function M is minimized by looking at the peak shape, peak width and preferred orientation for this end a Gaussian distribution is used. For further reading into this refinement I would recommend Rietveld Refinement guidelines by McCusker et al. [34].
In the crystallographic field software has been developed to perform refinements on experimental diffraction data, in this thesis the program Fullprof was used [35]. Subsequently in this thesis we will limit ourselves to full profile structure refinement of the cell parameters, this means we start from structure data found in Pearson's Crystal Data [32] and solely refine the cell parameters and not the atomic positions.

LeBail fit

A simpler way of calculating cell parameters from diffraction patterns is found in the Le Bail fitting procedure [36]. Where the Rietveld refinement requires the input extensive variables such as the atomic positions the Le Bail fitting procedure generates its pattern solely from the space group. This means that whilst the procedure is limited in its possibilities it is very desirable when solely calculating the cell parameters as it requires less input and is altogether less complicated. However the required input files of this fit gave many issues during a long duration of this work so was not always used.

2.2.2. Infrared spectroscopy

Infrared spectroscopy can be used to determine phosphates bonds and their orientation. [37]. To this end we needed a reliable method to produce and measure our samples. For this purpose the Shimadzu FTIR-8300 was used and samples were prepared by mixing with potassium bromide in a 0.1% ratio of sodium zirconium phosphate (NZP) and pressing into pellets at 10 MPa using a hydraulic press. The ratio was experimentally uncovered by multiple measurements at different ratios as shown in figure 2.6.

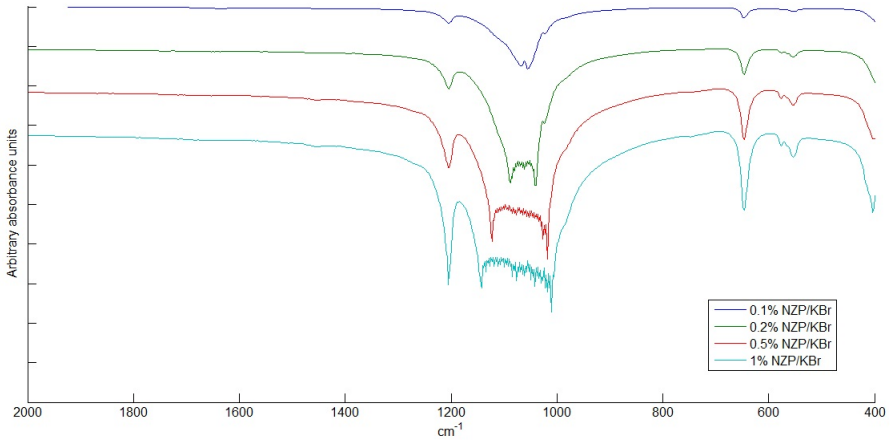

Figure 2.6: IR spectroscopy patterns of samples of sodium zirconium phosphate and potassium bromide in different ratios.

For all higher ratios than 0.1% oversaturation of the spectra was observed. At the concentration of 0.1% the IR spectra was obtained as shown in literature [38].

2.2.3. Leaching Testing

If any ceramic material is to be used as a waste matrix for radioactive isotopes we will need to be sure of its chemical stability and durability. One of the important parameters is the leaching rate which shows the leachability of the individual ions into a solution. This parameter needs to be as low as possible to avoid the release of radionuclides.
To determine the leaching rate in our case we use the Soxhlet apparatus. In this method there is a constant flow of fresh leachant, modelling a worst case scenario as the flooding of a facility. The experimental set-up involves a round-bottom flask, a heater, a Soxhlet and cooler and is shown in figure 2.7.
The solution used is 250 mL of deionised water which is boiled by the heater and condensated in the cooler making it accumulate in the Soxhlet, where the pellet is placed, until it reaches the maximum volume of the Soxhlet and flows out back into the round-bottom flask. Probes are taken from the round-bottom flask every few days which are measured by ICP-OES (Inductively Coupled Plasma Optical Emission Spectrometry) to determine ion concentrations. These measured concentrations can thereafter be used to calculate the normalized mass loss and subsequently the leaching rate by the formulas shown in equations 2.3 and 2.4.

$$NL_i = \frac{c_i V}{f_i SA} \tag{2.3}$$

$$R_i = \frac{dNL_i}{dt} \tag{2.4}$$

In these equations NL_i is the normalized mass loss of species i in $\frac{\mathrm{mg}}{\mathrm{m}^2}$, c_i is the concentration of species i in $\frac{mg}{L}$, V is the solution volume in L, f_i is the mass fraction of element i in the unleached solid, SA is the surface area of the solid in m^2 and R_i is the leaching rate in $\frac{\mathrm{mg}}{\mathrm{m}^2\mathrm{d}}$.

Figure 2.7: Experimental set-up of the Soxhlet leaching test.

ICP-OES

Inductively coupled plasma optical emission spectrometry (ICP-OES) is an analytical technique that can be used to determine trace mixtures of ions in a solution by using inductively coupled plasma that creates excited atoms that emit characteristic wavelength electromagnetic radiation [39]. The machine used in this work is Perkin Elmer Optima 4300 DV.
For the calculation of concentrations using this method the machine requires standards with know concentrations to this end standards were made containing all ions to be tested: cesium, strontium, zirconium, iron and phosphorus at concentrations of 1, 5, 10 and 20 $\frac{\mathrm{mg}}{\mathrm{L}}$.

2.2.4. Differential thermal analysis and thermogravimetric analysis

Differential thermal analysis (DTA) is a thermoanalytic technique that studies thermal cycles in a material [40]. In DTA the material and a reference undergo the same thermal treatment, where the reference is inert and does not change the material might for example crystallize or decompose leading to endo- or exothermal peaks that can be measured. These peaks give an insight in among other things the thermal stability, and composition of the studied material. Simulatanously thermogravimetric analysis (TGA) is done, this is a thermoananaltyic technique that measures the change of physical and chemical properties with increasing temperature [41]. This technique is used to study the mass loss as a function of temperature to study these physical and chemical changes. In this work the combined measurement is done using the Setarom Setsys evo 1750.

3

Results and Discussion

3.1. Cesium and Strontium containing NZP-type ceramics

3.1.1. Phase formation in the series $Cs_xSr_{(1-x)/2}[Zr_2(PO_4)_3]$

Five samples ranging from x=0 to x=1 of this series were synthesized, via the mechanochemical synthesis route described in section 2.1.1 using consecutive heating at 600 and finally 1000 °C, and analysed. The powder diffraction patterns are shown in figure 3.1.

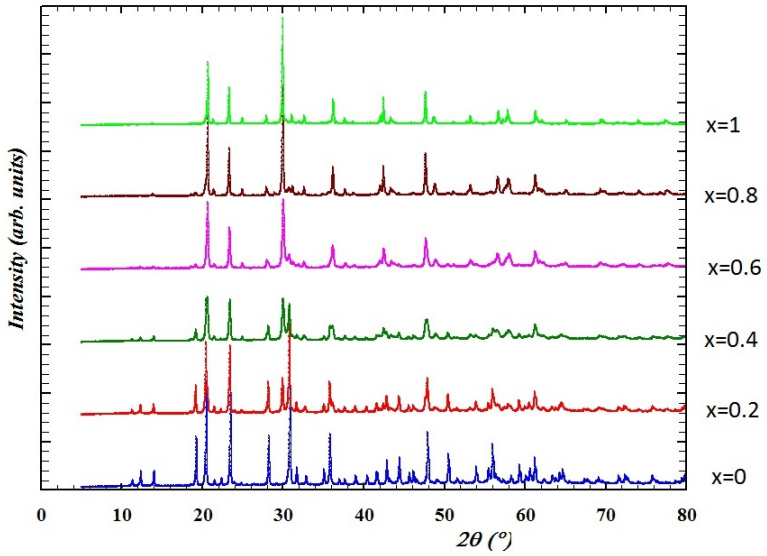

Figure 3.1: Powder diffraction patterns of the samples in series $Cs_xSr_{(1-x)/2}[Zr_2(PO_4)_3]$.

In this series the two end members, $Cs[Zr_2(PO_4)_3]$ and $Sr_{0.5}[Zr_2(PO_4)_3]$ are known to crystallize in the NZP-type [42] with respective space groups $R\bar{3}c$ and $R\bar{3}$. The calculations of the cell parameters of these end members were performed using this published data obtained from Pearson's Crystal Data [32] as can be seen in figures 3.2 and 3.3. What can be seen most prominently is that $Sr_{0.5}[Zr_2(PO_4)_3]$ shows two additional peaks in the low 2θ region with h=k=0 and l=1 that $Cs[Zr_2(PO_4)_3]$ does not. This is explained by the difference in space groups between the two end members. Where $Cs[Zr_2(PO_4)_3]$ has completely filled M1 positions and thus has a mirror plane in c, $Sr_{0.5}[Zr_2(PO_4)_3]$ does not, as strontium cations only fill half of the M1 positions. This decrease in symmetry gives $Sr_{0.5}[Zr_2(PO_4)_3]$ the space group $R\bar{3}$ whilst $Cs[Zr_2(PO_4)_3]$ crystallizes in space group $R\bar{3}c$. Furthermore in both end members an admixture in the form of zirconium pyrophosphate is seen at 21° whilst this is clear in figure 3.2 in figure 3.3 this peaks overlaps with an NZP peak but the presence of this admixture expresses itself at 31° by the small peak indicated by the asterisk.

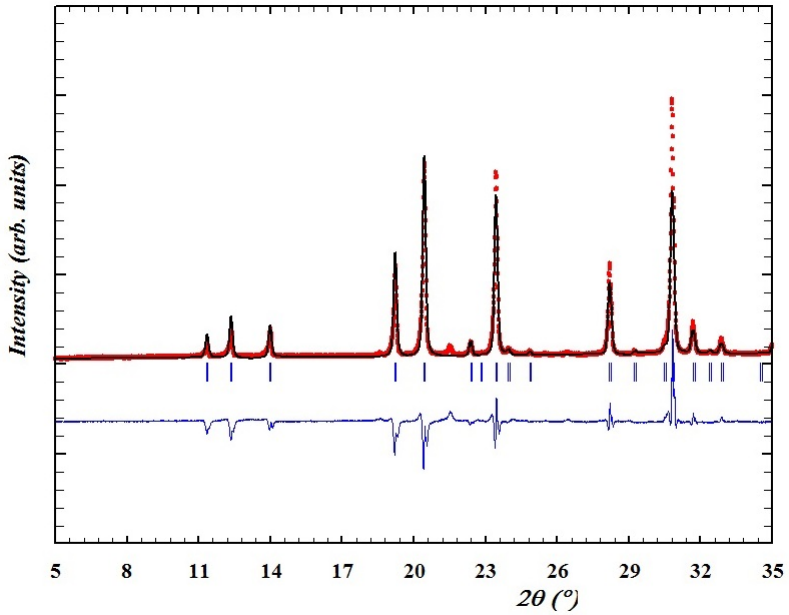

Figure 3.2: Part of the full profile fit of the sample of series $Cs_xSr_{(1-x)/2}[Zr_2(PO_4)_3]$ with x=0, the experiment data are shown in red, theoretical data in black and the difference given in blue.

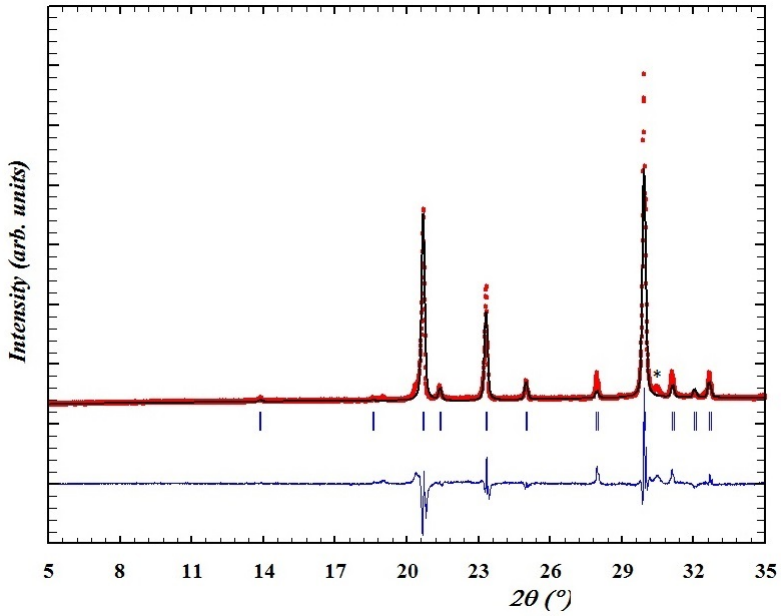

Figure 3.3: Part of the full profile fit of the sample of series $Cs_xSr_{(1-x)/2}[Zr_2(PO_4)_3]$ with x=1, shown are the experiment data in red, theoretical data in red and the difference given in blue.

Knowing NZP-phases were formed cell parameter calculations were done on the other samples of the series, however when a single phase model is used on any of the intermediate samples the theoretical fit mismatches some peaks as can be seen in the case of x=0.6 as shown in figure 3.4. For this model the spacegroup of the cesium NZP phase was used, $R\bar{3}c$, when refined using the LeBail fit we find these mismatched peaks that belong to neither the NZP phase nor zirconium pyrophosphate.

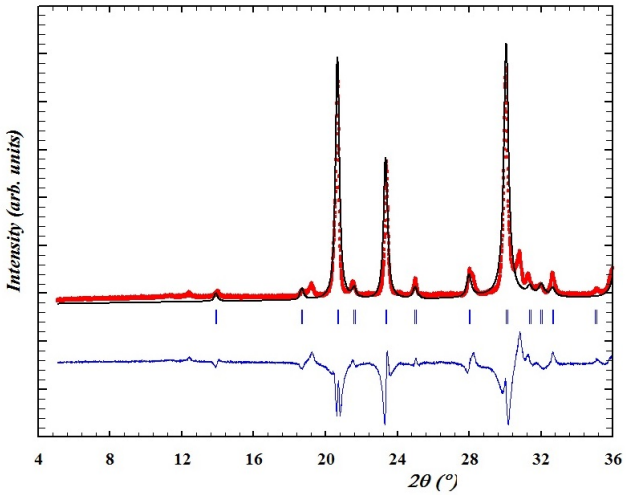

Figure 3.4: Part of the single phase full profile fit of the sample of series $Cs_xSr_{(1-x)/2}[Zr_2(PO_4)_3]$ with x=0.6. The experimental data is shown in red and the theoretical in black, the blue bars indicate the positions of the bragg peaks and the blue curve shows the difference.

Due to the poor fit of this single phase model, a two phase model was used instead. This model is based on the coexistence of two individual crystal phases of the end members, a similar mechanical mixture was found by Bahl et al. [43] for Ca- and $BaMoO_4$ on borosilicate glass. Cell parameter calculations done with this profile showed a better fit as can be seen in figure 3.5, a two phase full profile fitting done on the sample with x=0.6.

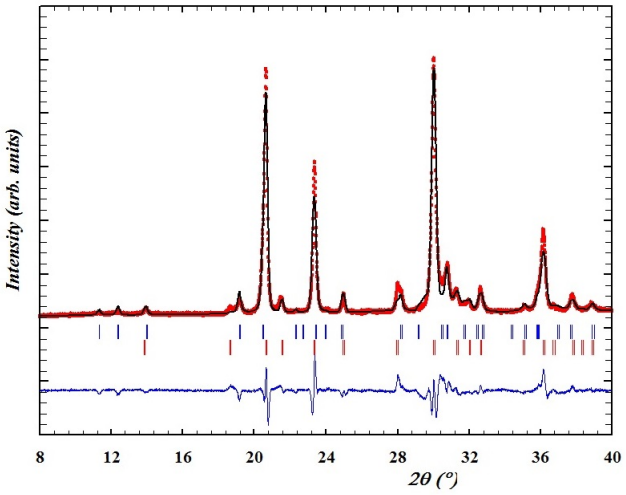

Figure 3.5: Part of the two phase full profile fit of the sample of series $Cs_xSr_{(1-x)/2}[Zr_2(PO_4)_3]$ with x=0. The experimental data is shown in red and the theoretical in black, bragg peaks of the phases are shown in blue and red bars for cesium and strontium-rich phases respectively and the difference curve in blue.

A two phase full profile fitting procedure was done on every sample within this series, the resulting cell parameters of these calculations are shown in table 3.1. Both phases are represented by their end members, $Cs[Zr_2(PO_4)_3]$ for the Cs-rich phase and $Sr_{0.5}[Zr_2(PO_4)_3]$ for the Sr-rich phase.

Table 3.1: Resulting cell parameters from a full profile fitting procedure for the two phase model, a strontium-rich and cesium-rich phase.

x	a Sr-rich phase (Å)	c Sr-rich phase (Å)	a Cs-rich phase (Å)	c Cs-rich phase (Å)
0	8.687 ± 0.005	23.38 ± 0.01	N.A.	N.A.
0.2	8.678 ± 0.002	23.42 ± 0.01	8.588 ± 0.006	24.83 ± 0.03
0.4	8.675 ± 0.004	23.46 ± 0.02	8.600 ± 0.003	24.74 ± 0.02
0.6	8.679 ± 0.009	23.49 ± 0.04	8.598 ± 0.002	24.74 ± 0.01
0.8	8.71 ± 0.01	23.38 ± 0.07	8.591 ± 0.001	24.827 ± 0.008
1	N.A.	N.A.	8.585 ± 0.002	24.914 ± 0.009

In order to look for a correlation or dependency the cell parameters of both phases have been plotted against x shown in figure 3.6. Additionaly the volume of the two unit cells are shown in figure 3.7.

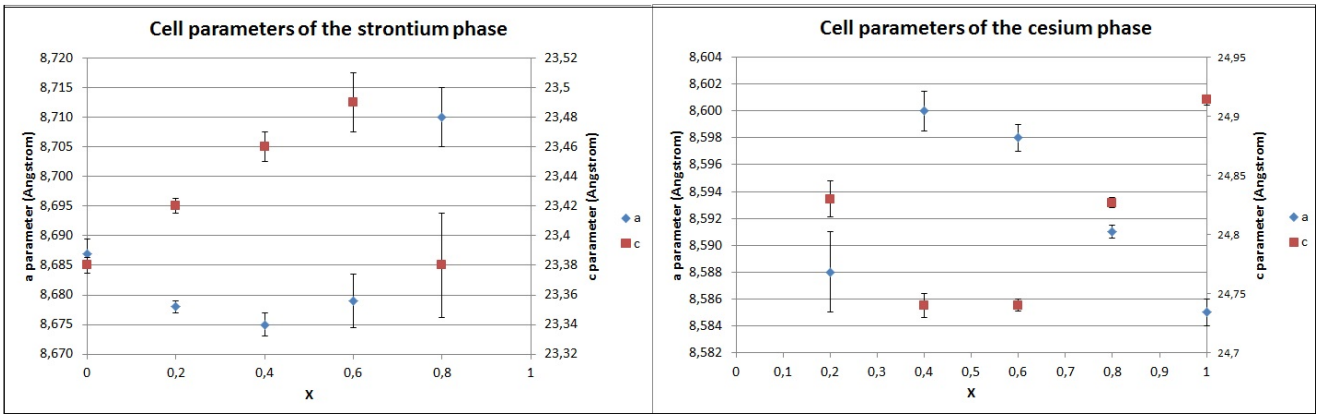

Figure 3.6: Cell parameters of both NZP phases plotted against the stoichiometric variable x, errors are plotted showing the uncertainty of the calculations.

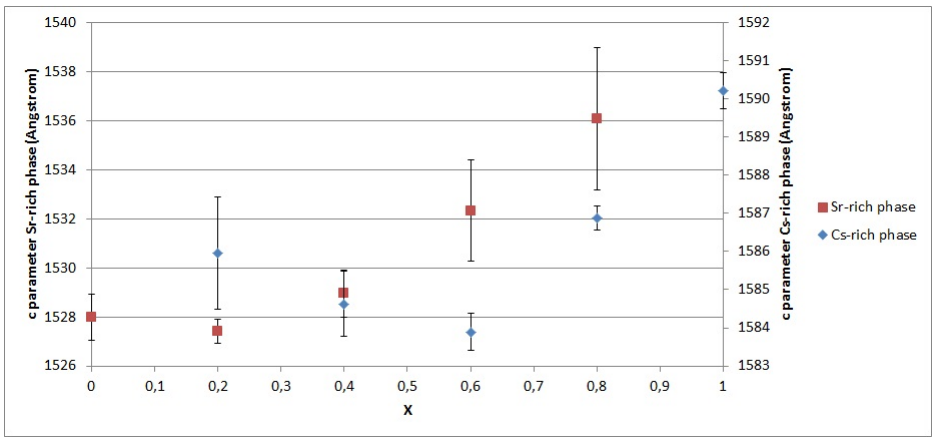

Figure 3.7: Volume of the unit cell of both Sr and Cs-rich phases plotted against the stoichiometric variable x, errors are plotted showing the uncertainty of calculations

.

Vegard's law states that the lattice parameters of a solid solution is equal to a rule of mixtures of the individual lattice parameters [44], the formula is shown in equation 3.1. In this equation we discern two species, A and B that are mixed in ratio x and have respective lattice parameters a_A and a_B.

$$a_{A_{1-x}B_x} = (1-x)a_A + xa_B \tag{3.1}$$

This equation dictates a linear relationship between the cell parameters and the ratio x. So in the case of full miscibility we would get a straight line between x=0 and x=1, this however is not the case.

What we find is that for the a parameter there is a slight decrease for the strontium phase at the first samples, x=0.2 and arguably x=0.4 hereafter however we see an increase in this parameter. For the c parameter we see a slight increase for the samples x=0.2,0.4 and 0.6 before decreasing. A possible explanation could be a slight solubility between the phases, cesium is a bigger cation than strontium, at 1.67 Å and 1.18 Å respectively in our case of VI coordination, which means the cell would expand as seen by the change of volume shown in figure 3.7. This however does not explain the sudden change in relation at higher values of x, but this might be explained by the limited presence of strontium meaning there is no solubility between the phases and causing strontium to return to its pure state as seen by the cell parameters returning to the x=0 value. When we look at the other phase, of cesium, we find a similar situation. When approaching the cesium phase from x=1, its pure form, a increases with decreasing x up until x=0.4 at which point it returns to the original value. The opposite happens for the c parameter which decreases up to x=0.4 at which point it increases once again. Likely we are dealing with the same situation, meaning some strontium is occupying cesium's M1 positions causing, due to strontium's smaller size, the c parameter to decrease and as a result a parameter to increase.

3.1.2. Phase formation in the series $Sr_{1-(x/2)}[Zr_{1+x}Fe_{1-x}(PO_4)_3]$

The samples of this series followed the route of synthesis explained in section 2.1.1 with heating steps of 600 and 1000 °C. Powder diffraction patterns of these samples are shown in figure 3.8.

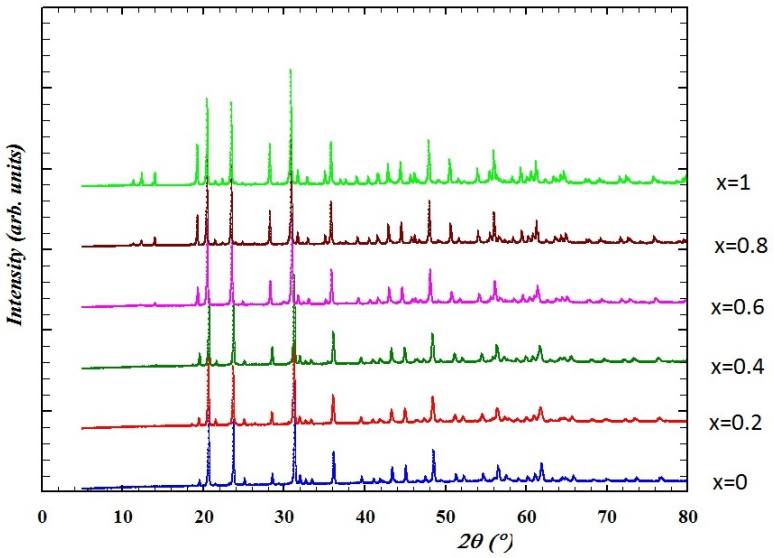

Figure 3.8: Powder diffraction patterns of the series $Sr_{1-(x/2)}[Zr_{1+x}Fe_{1-x}(PO_4)_3]$

Similar to the series studied in section 3.1.1 there should be a loss of symmetry between the end member $Sr[ZrFe(PO_4)_3]$ and $Sr_{0.5}[Zr_2(PO_4)_3]$ because both are known to crystallize in space groups $R\bar{3}c$ and $R\bar{3}$ respectively. For both end members cell parameters were calculated using their respective structure models found in Pearson's Crystal Data [32] as shown in figure 3.9. Additionaly $Sr_{0.5}[Zr_2(PO_4)_3]$ was also an end member of the series described in section 3.1.1 and the refinement plot for this end member can be found in that section.

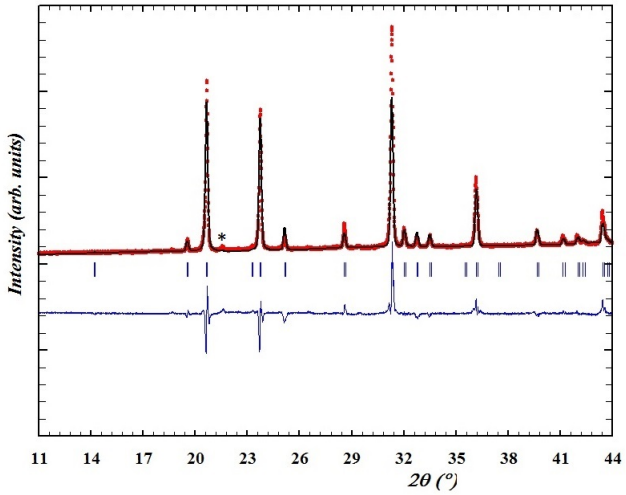

Figure 3.9: Part of the full profile fit of the sample of series $Sr_{1-(x/2)}[Zr_{1+x}Fe_{1-x}(PO_4)_3]$ with x=0. Experimental pattern is shown in red whilst the black lines forms the theoretical diffraction pattern, the blue curve shows the difference between the two.

Like the series described in section 3.1.1 a small admixture of zirconium pyrophosphate is present in every sample, the amount is however very little meaning it hardly contributes to the pattern as can be seen in the full profile fits by the small peak at approximately 21° indicated by the asterisk. When a single phase full profile fit is used on the intermediate samples we get a good fit as shown by figure 3.10. The symmetry change in this series causes the end members to have different space groups

meaning x=0 till x=0.6 were fitted using $Sr[ZrFe(PO_4)_3]$'s space group of $R\bar{3}c$ whilst x=0.8 and 1 were done with the space group of $Sr_{0.5}[Zr_2(PO_4)_3]$, $R\bar{3}$, determined by the presence of the peaks around 10-15°.

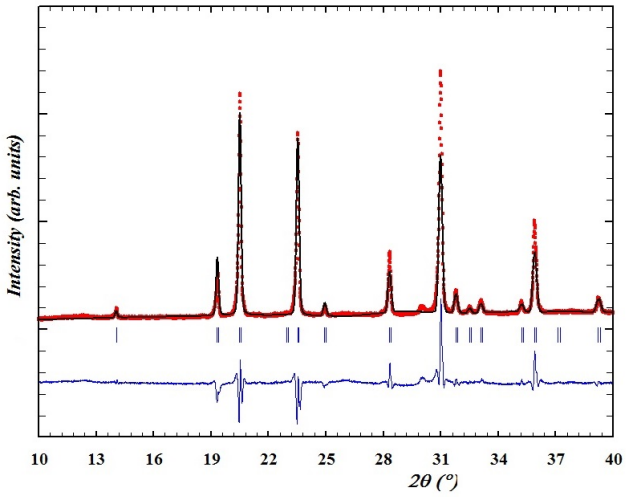

Figure 3.10: Part of the full profile fit of the sample of series $Sr_{1-(x/2)}[Zr_{1+x}Fe_{1-x}(PO_4)_3]$ with x=0.6. Experimental diffraction pattern is shown in red, the theoretical pattern in black and the difference of the two in blue

Unlike the series described in 3.1.1 all the NZP peaks belong to one structure described by two different space groups giving us reason to belief there is in fact the formation of a solid solution. This is further proven by full profile fits done on the other intermediates in this series. The resulting cell parameters from these calculations are shown in table 3.2.

Table 3.2: Resulting cell parameters from a full profile fitting procedure for a single phase model.

x	a (Å)	c (Å)
0	8.598 ± 0.002	22.928 ± 0.008
0.2	8.611 ± 0.002	23.00 ± 0.01
0.4	8.644 ± 0.003	23.08 ± 0.01
0.6	8.661 ± 0.002	23.22 ± 0.01
0.8	8.675 ± 0.006	23.27 ± 0.02
1	8.687 ± 0.005	23.38 ± 0.01

Both cell parameters seem to follow a linear trend with regards to x, this linear trend is shown in figure 3.11. Additionally the volume of the unit cell calculated with these parameters is shown in figure 3.12.

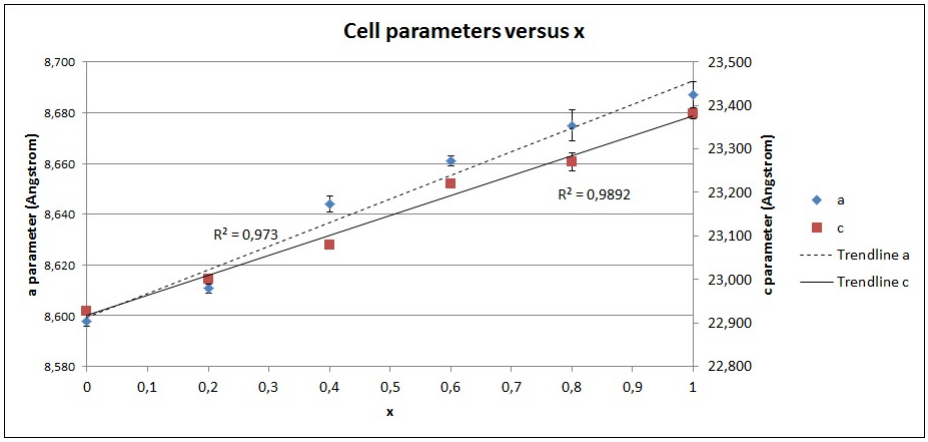

Figure 3.11: Plot of the cell parameters against the stoichiometric x for samples of series $Sr_{1-(x/2)}[Zr_{1+x}Fe_{1-x}(PO_4)_3]$

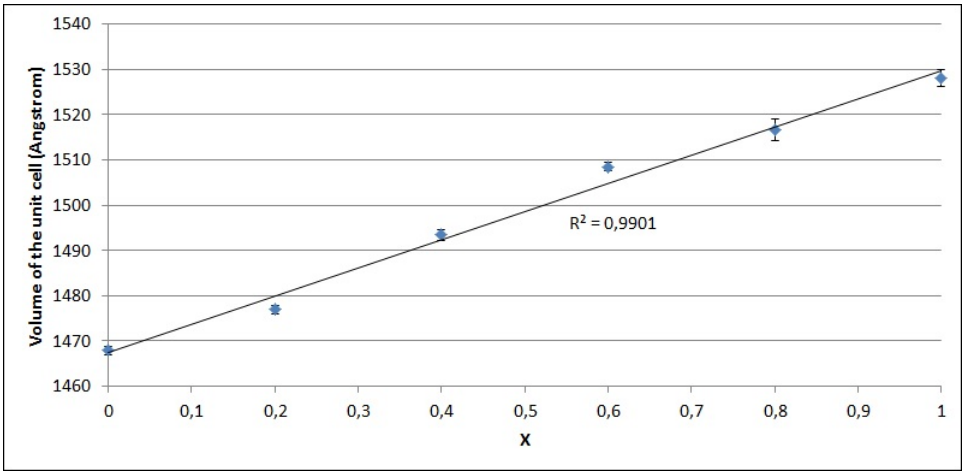

Figure 3.12: Plot of the unit cell volume against the stoichiometric x for samples of series $Sr_{1-(x/2)}[Zr_{1+x}Fe_{1-x}(PO_4)_3]$

This linear relation confirms the existence of a solid solution. With an increase in x, iron is replaced by zirconium in the framework. Zirconium has a cationic radii of 0.72 Å whilst iron's is 0.645 Å. Logically when zirconium replaces iron the framework expands, as is shown by the change of volume in figure 3.12. Also with increasing x more M1 positions become vacant which would causing repulsion forces to increase between the framework cations and anions negating the change from the removal of strontium.

3.1.3. Phase formation in the series $Cs_xSr_{1-(x/2)}[Zr_{1+x}Fe_{1-x}(PO_4)_3]$

Samples of this series were first synthesized following the mechanochemical route explained in section 2.1.1 with heating temperatures of 600 and 1000 °C. The powder diffraction patterns of these samples are shown in figure 3.13

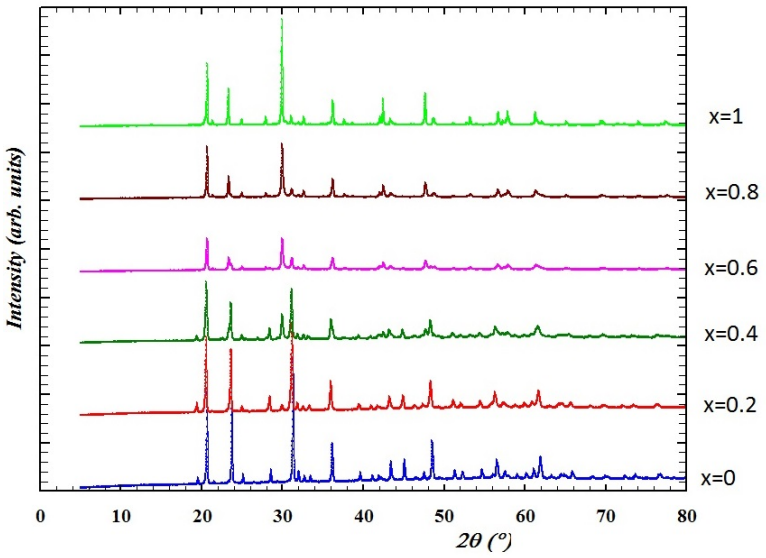

Figure 3.13: Powder diffraction patterns of the series $Cs_xSr_{1-(x/2)}[Zr_{1+x}Fe_{1-x}(PO_4)_3]$

The end members of this series have already been analyzed as part of the series studied in sections 3.1.1 and 3.1.2, as seen in figure 3.9 for $Sr[ZrFe(PO_4)_3]$ and 3.3 for $Cs[Zr_2(PO_4)_3]$ these crystallize as NZP. When we look at the diffraction patterns however the intermediates exhibit the same splitting of peaks as the series in section 3.1.1, this gives us an indication that we are once again dealing with two individual phases. This hypothesis is further proven by a single phase full profile fit done on sample x=0.6, $Cs_{0.6}Sr_{0.4}[Zr_{1.6}Fe_{0.4}(PO_4)_3]$ shown in figure 3.14, for this fit the structure data of $Cs[Zr_2(PO_4)_3]$ was used.

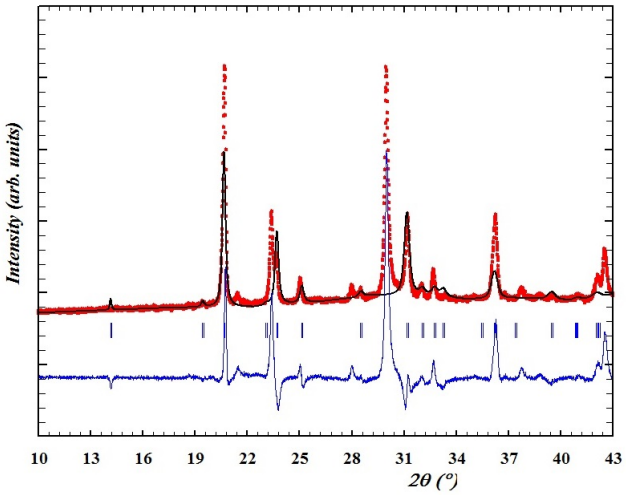

Figure 3.14: Part of the single phase full profile fit of the sample of series $Cs_xSr_{1-(x/2)}[Zr_{1+x}Fe_{1-x}(PO_4)_3]$ with x=0.6. The experimental pattern is shown in red, theoretical pattern in black and the difference in blue.

However when a two phase model is used on the same sample the resulting fit is much better as shown in figure 3.15. For this model we use the two end members as separate phases, being $Sr[ZrFe(PO_4)_3]$ and $Cs[Zr_2(PO_4)_3]$.

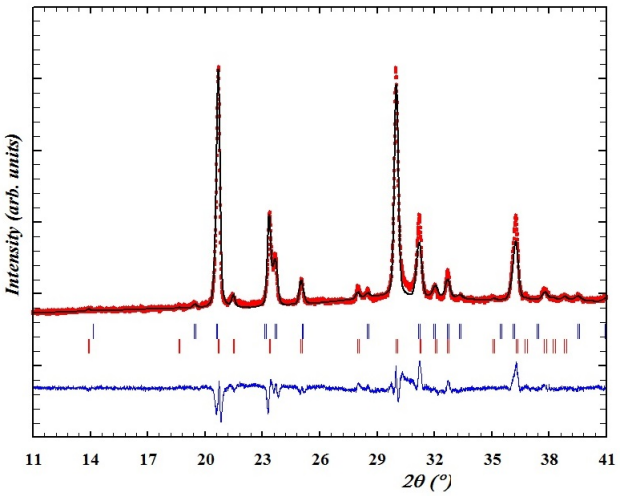

Figure 3.15: Part of the two phase full profile fit of the sample of series $Cs_xSr_{1-(x/2)}[Zr_{1+x}Fe_{1-x}(PO_4)_3]$ with x=0.6. The experimental pattern is shown in red, theoretical pattern in black and the difference in blue.

Using the two phase model, of a strontium and cesium-rich phase, cell parameters were calculated for every sample in this series, the results are shown in table 3.3.

Table 3.3: Resulting cell parameters from a full profile fitting procedure using the two phase model, a strontium and cesium phase.

x	a Sr-rich phase (Å)	c Sr-rich phase (Å)	a Cs-rich phase (Å)	c Cs-rich phase (Å)
0	8.598 ± 0.002	22.928 ± 0.008	N.A.	N.A.
0.2	8.633 ± 0.004	23.00 ± 0.01	8.65 ± 0.01	23.05 ± 0.05
0.4	8.629 ± 0.006	23.07 ± 0.02	8.583 ± 0.008	24.80 ± 0.03
0.6	8.615 ± 0.008	23.06 ± 0.04	8.579 ± 0.002	24.82 ± 0.01
0.8	8.63 ± 0.02	23.04 ± 0.09	8.581 ± 0.001	24.83 ± 0.01
1	N.A.	N.A.	8.585 ± 0.002	24.914 ± 0.009

These cell parameters are plotted in figure 3.16. Additionaly the volume of the unit cell is given in figure 3.17.

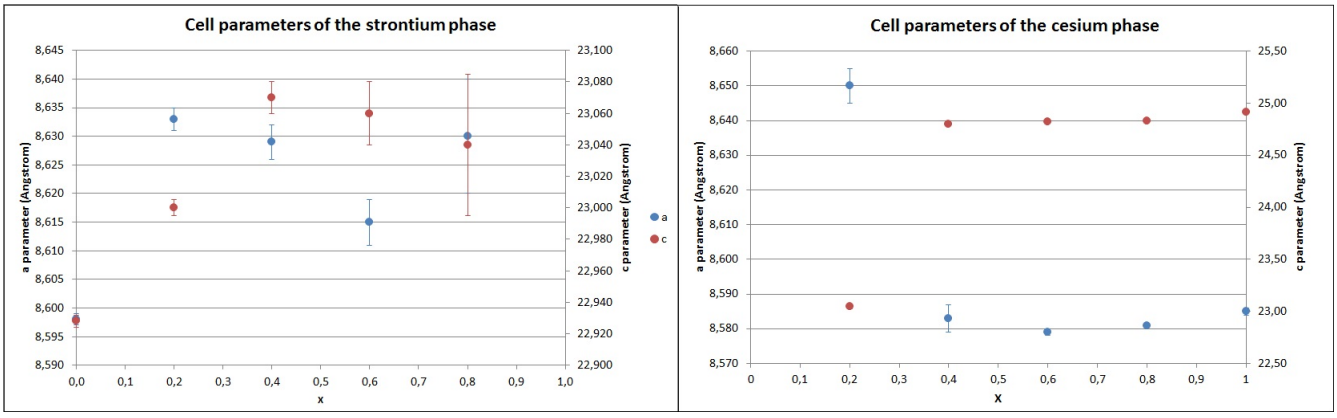

Figure 3.16: Plot of the cell parameters of both phases in the series $Cs_xSr_{1-(x/2)}[Zr_{1+x}Fe_{1-x}(PO_4)_3]$.

Looking at the cell parameters of the strontium phase one can notice that with the exception of x=0, the parameters stay relatively constant, the slight changes that do occur are insignificantly small. We

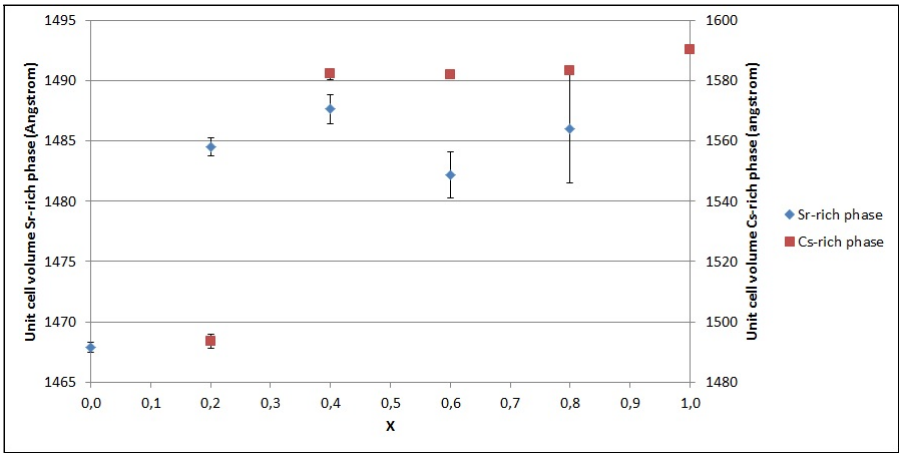

Figure 3.17: Plot of the unit cell volume of both phases in the series $Cs_xSr_{1-(x/2)}[Zr_{1+x}Fe_{1-x}(PO_4)_3]$.

observe a similar situation for the parameters of the cesium phase when we exclude x=0.2. A possible explanation for the strontium phase could be the slight miscibility of zirconium which is replacing iron in the framework. This would cause strontium to leave the M1 position but as seen in the series in section 3.1.2 the cell parameters would both increase. For the cesium phase there might be no miscibility until x=0.2 at which the dominant strontium takes up some of the M1 positions which would make c-parameter to increase and subsequently decrease the a-parameter. This is further proven by the volume of the unit cell in figure 3.17.

Possibly the two phase formation was caused by the high temperature of crystallization of 1000 °C, at this temperature the solid solution might have decomposed under the formation of the two individual phases. To further study this all samples of this series were synthesized once more via the mechanochemical route described in section 2.1.1 but at a lower temperature of 600 and subsequently 800 °C. The powder diffraction patterns of these samples are shown in figure 3.18.

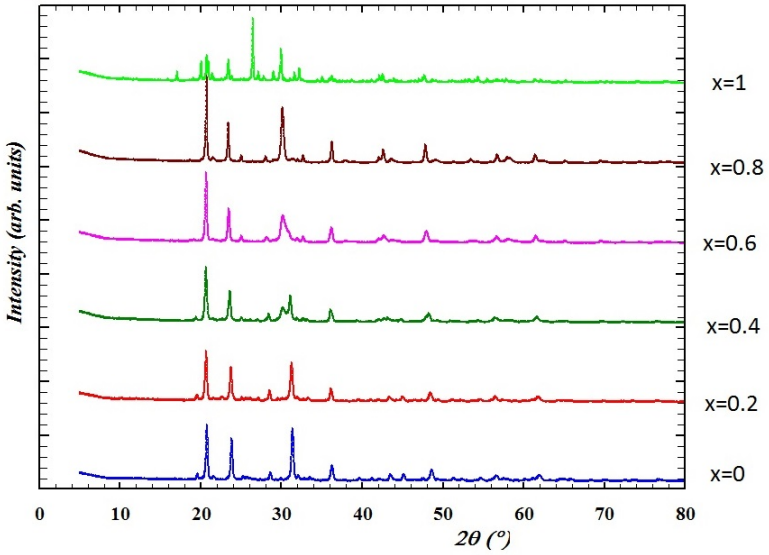

Figure 3.18: Powder diffraction patterns of the series $Cs_xSr_{1-(x/2)}[Zr_{1+x}Fe_{1-x}(PO_4)_3]$, heated at 800 °C.

When the powder diffraction patterns of these new samples are compared to ones heated at 1000 °C we see little to no changes in peak positions and relative intensity as shown in figure 3.19 an example the sample of series $Cs_xSr_{1-(x/2)}[Zr_{1+x}Fe_{1-x}(PO_4)_3]$ with x=0.4, where in blue is the sample heated at 1000 °C and in red the sample heated at 800 °C.

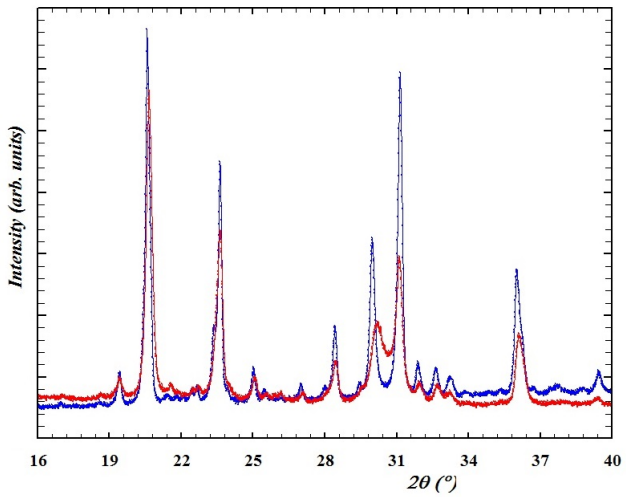

Figure 3.19: Part of the powder diffraction patterns of the sample of series $Cs_xSr_{1-(x/2)}[Zr_{1+x}Fe_{1-x}(PO_4)_3]$ with x=0.4, synthesized at two different temperatures, 1000°C (blue) and 800° (red).

From this figure we can observe that the intensity of the sample crystallized at 800 °C is less than the sample crystallized at 1000 °C and since the same instrumentation was used we can conclude that the crystallinity is less. Besides this decrease in crystallinity little difference can be found between the two patterns meaning these samples also crystallized into two individual phases.
One more attempt was made to synthesize a solid solution, namely using the Pechini method of synthesis to see if the homogenization can promote the formation of a solid solution, explained in section 2.1.1, with heating steps of 600°C and 800°. For this method sample x=0.6 was used because this best represents the UREX waste stream composition [4]. The resulting powder diffraction pattern is shown in figure 3.20

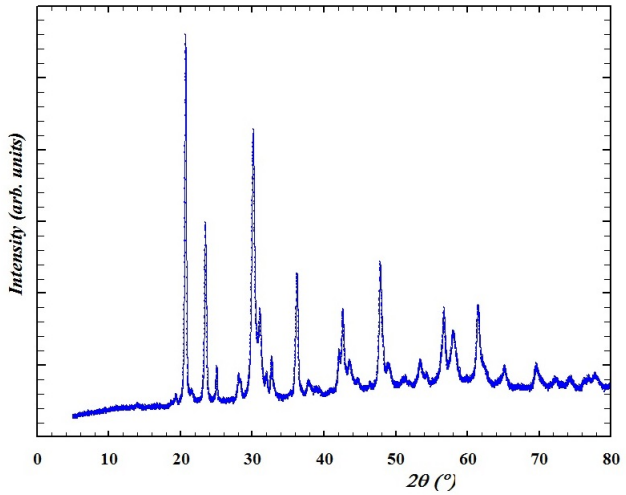

Figure 3.20: Powder diffraction pattern of sample x=0.6, $Cs_{0.6}Sr_{0.4}[Zr_{1.6}Fe_{0.4}(PO_4)_3]$, synthesized via the Pechini method.

When this pattern is compared to the sample synthesized via the mechanochemical route at a 1000 °C we find that not much has changed, as can be seen in figure 3.21. There is an increase in intensity but also in background, making it unclear whether the crystallinity has actually improved which makes sense as a lower temperature was used. More importantly however we see the same splitting of peaks as the mechanochemical sample proving that this method also formed no solid solution. As is shown by the full profile fit done on mechanochemical sample shown in figure 3.15

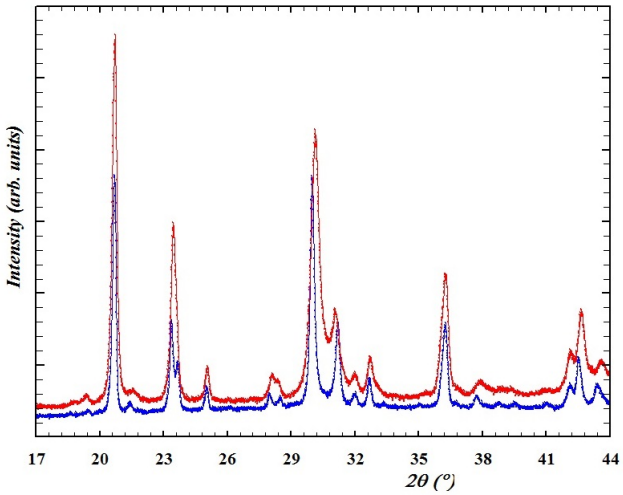

Figure 3.21: Powder diffraction patterns of the sample of series $Cs_xSr_{1-(x/2)}[Zr_{1+x}Fe_{1-x}(PO_4)_3]$ with x=0,6, synthesized via mechanochemical in blue and Pechini method in red.

Samples of this series were also synthesized earlier by Priya Jagai [23] in that work the existence of a solid solution was concluded. The mechanochemical method of synthesis was used as described in section 2.1.1 with heating of 1000 °C, the powder diffraction patterns of these samples are shown in figure 3.22.

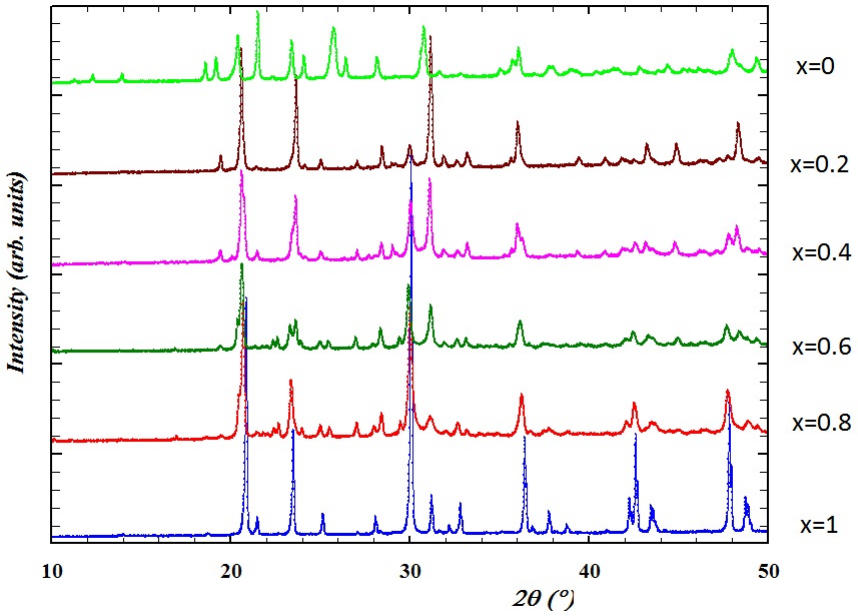

Figure 3.22: Powder diffraction patterns of the series $Cs_xSr_{1-(x/2)}[Zr_{1+x}Fe_{1-x}(PO_4)_3]$

Whilst both end members show their respective diffraction pattern albeit with admixtures, the intermediates show the same splitting of peaks as the samples synthesized in this thesis. This gives us reason

an indication that there is no complete solid solution but again a mixture of two separate phases. This is further proven by comparing the powder diffraction patterns as is done for sample x=0.6 in figure 3.23. In this figure we see the same splitting of peaks belonging to the NZP phases in both samples which proves the formation of two individual phases as shown by the earlier refinement done on this sample shown in 3.15.

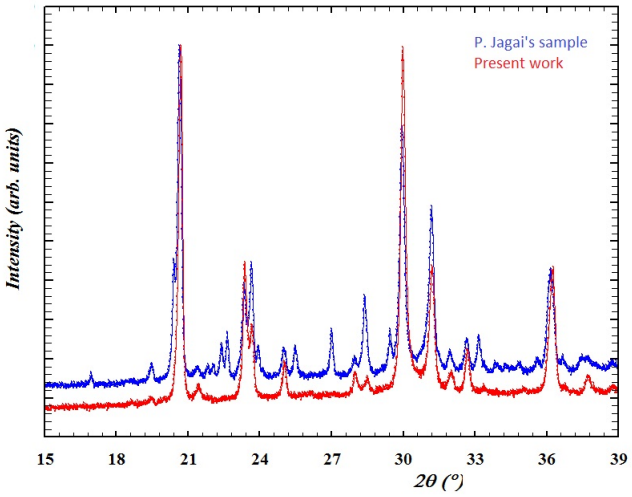

Figure 3.23: Powder diffraction patterns of the sample x=0.6, $Cs_{0.6}Sr_{0.4}[Zr_{1.6}Fe_{0.4}(PO_4)_3]$, synthesized by P.Jagai (in blue) and in the present work (in red).

Noticeable from this powder diffraction the sample synthesized by P. Jagai shows many admixtures which probably caused the misinterpetation in that work. The samples synthesized in the present research are much purer and allow for better phase studies. P. Jagai determined the presence of two main admixtures, namely zirconium pyrophosphate (ZrP_2O_7) and iron oxide Fe_2O_3. The presence of this iron oxide means there was an excess of iron during crystallization, meaning that the second NZP phase wasn't pure $Sr[ZrFe(PO_4)_3]$ but likely a solid solution between that structure and $Sr_{0.5}[Zr_2(PO_4)_3]$. The formation of solid solutions in the series $Sr_{1-(x/2)}[Zr_{1+x}Fe_{1-x}(PO_4)_3]$ was shown in section 3.1.2. This allows us to recalculate the actual composition of the strontium rich-phase.
Cell parameters of the strontium-rich phase were recalculated as shown in table 3.4 to determine the miscibility by relating the cell parameters to the linear trend found in section 3.1.2.

Table 3.4: Resulting cell parameters of the strontium-rich phase from a full profile fitting procedure for a two phase model obtained from the analysis of data of P.Jagai. And the calculated actual x value for the solid solution $Sr_{1-(x/2)}[Zr_{1+x}Fe_{1-x}(PO_4)_3]$.

intended x	a (Å)	c (Å)	actual x
0	8.600 ± 0.003	22.963 ± 0.008	0.05
0.2	8.638 ± 0.008	23.09 ± 0.02	0.40
0.4	8.65 ± 0.01	23.17 ± 0.03	0.55
0.6	8.61 ± 0.01	23.02 ± 0.04	0.17
0.8	8.66 ± 0.03	23.1 ± 0.1	0.53

The values for the first samples make sense as they show that the synthesis formed less $Sr[ZrFe(PO_4)_3]$ then expected which means there is an excess of iron that is free to crystallize as iron oxide. The values for x=0.6 and x=0.8 however show an increase in the $Sr[ZrFe(PO_4)_3]$ phase, this could be a result of the low content of strontium causing only very little strontium NZP phase to form which makes it difficult to determine the cell parameters and actual x value.

3.1.4. IR spectroscopy of cesium and strontium containing NZP type ceramics

IR measurements were done on all cesium and strontium containing NZP type samples discussed in sections 3.1.1 3.1.2 and 3.1.3.

The IR spectra of samples of the series $Cs_xSr_{(1-x)/2}[Zr_2(PO_4)_3]$ are shown in figure 3.24.

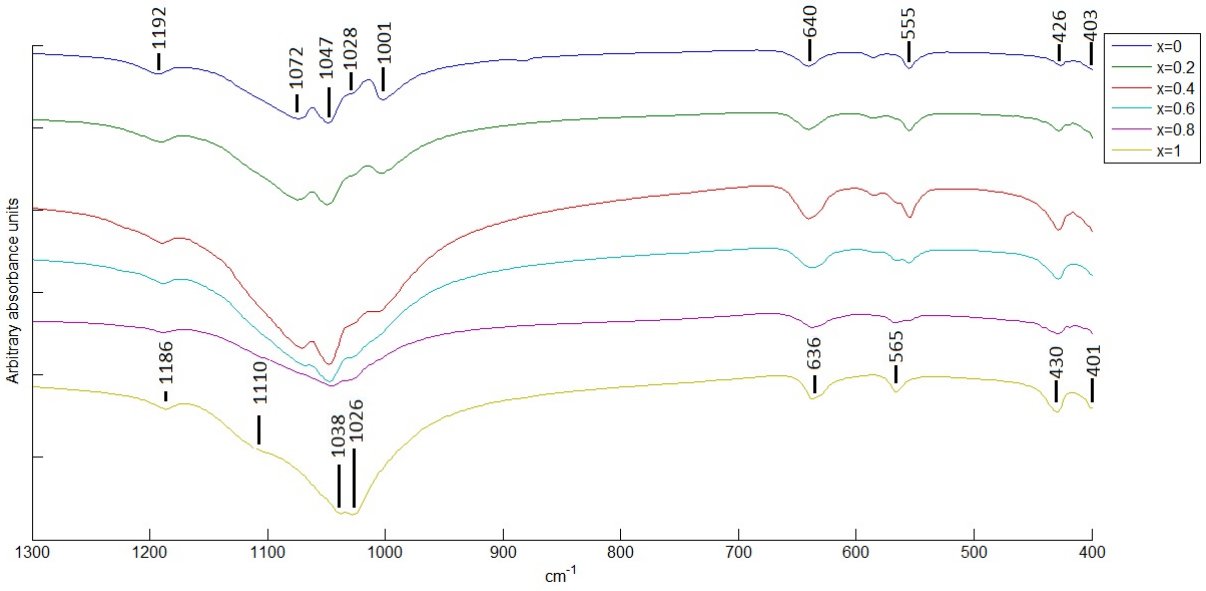

Figure 3.24: IR spectra of samples of the series $Cs_xSr_{(1-x)/2}[Zr_2(PO_4)_3]$

In all of the samples we observe peaks at the lower region of 400-670 cm^{-1} these are caused by the bending vibrations v_4 and v_2 of the phosphate ion $(PO_4)^{3-}$ [15]. The peaks at 1280-1000 cm^{-1} belong to the asymmetric stretching vibrations v_3 and symmetric stretching vibrations v_1 of the phosphate ion. We can observe the disappearance of some asymmetric stretching vibrations with increasing x which is a result of the increase of symmetry that comes with the change of space group from $R\bar{3}$ to $R\bar{3}c$ [45]. The two end members of this series $Cs[Zr_2(PO_4)_3]$ [46] and $Sr_{0.5}[Zr_2(PO_4)_3]$ [47] show spectra similar to earlier synthesized samples in literature.

IR spectra of the samples of the series $Sr_{1-(x/2)}[Zr_{1+x}Fe_{1-x}(PO_4)_3]$ are shown in figure 3.25.

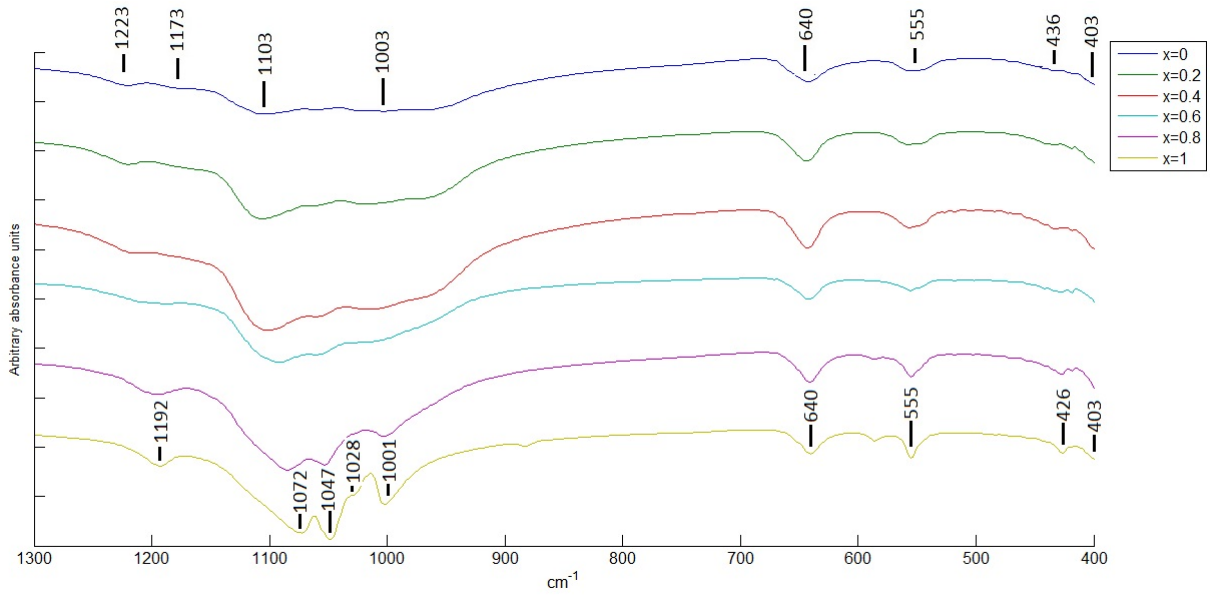

Figure 3.25: IR spectra of samples of the series $Sr_{1-(x/2)}[Zr_{1+x}Fe_{1-x}(PO_4)_3]$

In this series of samples we observe the same peaks as discussed before, coming from the bending and (a)symmetric stretching of the phosphate ion. With decreasing x we observe a disappearance of some asymmetric stretching vibrations as a result of the increase of symmetry due to the space group change from $R\bar{3}$ to $R\bar{3}c$ as also seen in the series $Cs_xSr_{(1-x)/2}[Zr_2(PO_4)_3]$. The end member of $Sr[ZrFe(PO_4)_3]$ shows a similar spectrum as the one defined in literature [48].

The IR spectra of the samples of the series $Cs_xSr_{1-(x/2)}[Zr_{1+x}Fe_{1-x}(PO_4)_3]$ are shown in figure 3.26.

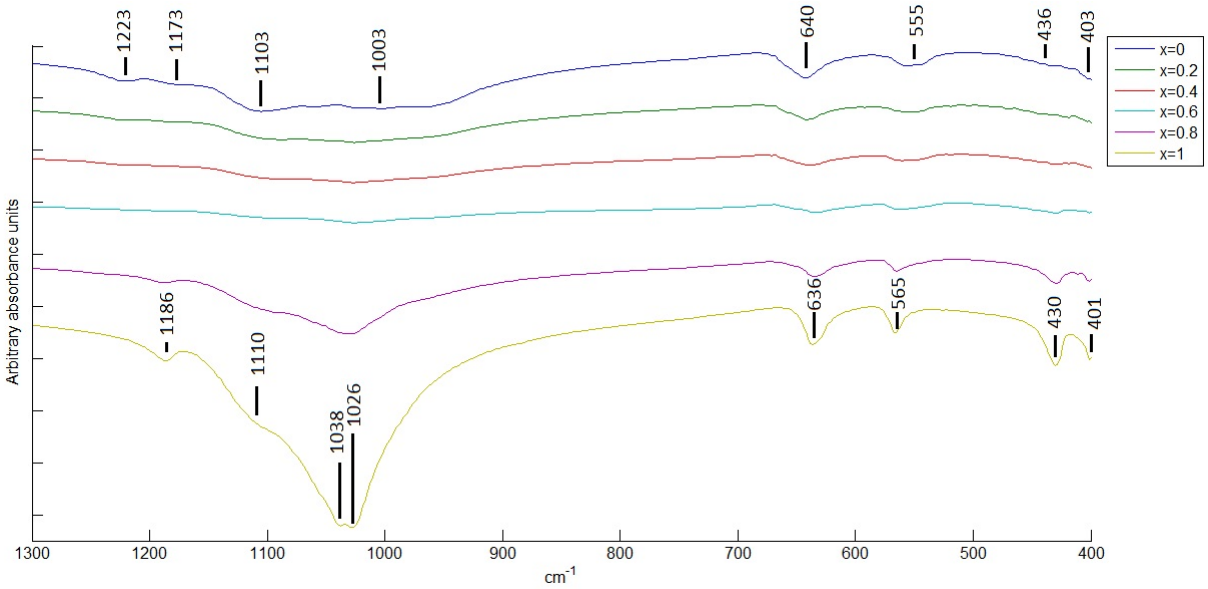

Figure 3.26: IR spectra of samples of the series $Cs_xSr_{1-(x/2)}[Zr_{1+x}Fe_{1-x}(PO_4)_3]$

In the samples of this series we see no change of peaks belonging to the asymmetric stretching vibration but we notice the spectra becoming more diffusive which can be a result of the different chemical formula. The spectra proves there is no difference in space group between the two end members of $Sr[ZrFe(PO_4)_3]$ and $Cs[Zr_2(PO_4)_3]$ as both were found to be $R\bar{3}c$.
All of the analysed samples however can be attributed to to the orthophosphate class [49].

3.1.5. Leachability of cesium and strontium containing NZP-type ceramics

Two samples were chosen to be analysed by leaching testing as described in 2.2.3, samples were chosen based on the best approximation of the UREX waste stream [4]. These samples are $Cs_{0.6}Sr_{0.4}[Zr_{1.6}Fe_{0.4}(PO_4)_3]$ and $Cs_{0.4}Sr_{0.3}[Zr_2(PO_4)_3]$, pellets of these samples were pressed and sintered at 1000 °C for 24 hours. Two experimental set-ups were built, one for each sample. The set-up for $Cs_{0.6}Sr_{0.4}[Zr_{1.6}Fe_{0.4}(PO_4)_3]$ had a 150 mL Soxhlet that renews solvent every two hours whilst $Cs_{0.4}Sr_{0.3}[Zr_2(PO_4)_3]$'s set-up had a 70 mL Soxhlet that renews solvent every one and a half hour.

Before starting the test porosity of the samples were determined, this was done by relating the actual density of pellet mass/volume to the theoretical density of the crystal lattices. The porosities of samples $Cs_{0.6}Sr_{0.4}[Zr_{1.6}Fe_{0.4}(PO_4)_3]$ and $Cs_{0.4}Sr_{0.3}[Zr_2(PO_4)_3]$ were found to be approximately 71 and 72% respectively, these were calculated by dividing the theoretical density of the unit cell by the actual density of the pellet but due to crystal imperfections there values are approximate. The surface area of the pellets were 415 and 452 mm^2 respectively.

Probes were taken after 2, 5, 9, 15 and 21 days which were measured by ICP-OES to determine the concentrations of ions.
The concentration of cesium for both samples was found to be under the detection limit of the used set-up, as cesium is difficult to ionize and needs a relatively high concentration to be measured. Additionaly the iron concentration also fell below the measurement threshold for sample $Cs_{0.6}Sr_{0.4}[Zr_{1.6}Fe_{0.4}(PO_4)_3]$. Subsequently the presence of both zirconium and phosphorus caused interference to their measured concentration, a possible explanation is the formation of a zirconium phosphate which would reduce the efficiency of ionization and thus also the intensity. This caused the internal standards to show lower concentrations than prepared leaving the calculated concentrations very inaccurate and unrepresentative.

The concentration of strontium in solution was successfully determined and used to calculate the leaching rate for both samples as shown in figure 3.27, $Cs_{0.6}Sr_{0.4}[Zr_{1.6}Fe_{0.4}(PO_4)_3]$ is in red and $Cs_{0.4}Sr_{0.3}[Zr_2(PO_4)_3]$ in blue. The mass fraction of strontium in these samples was 0.0671 and 0.0481 respectively.

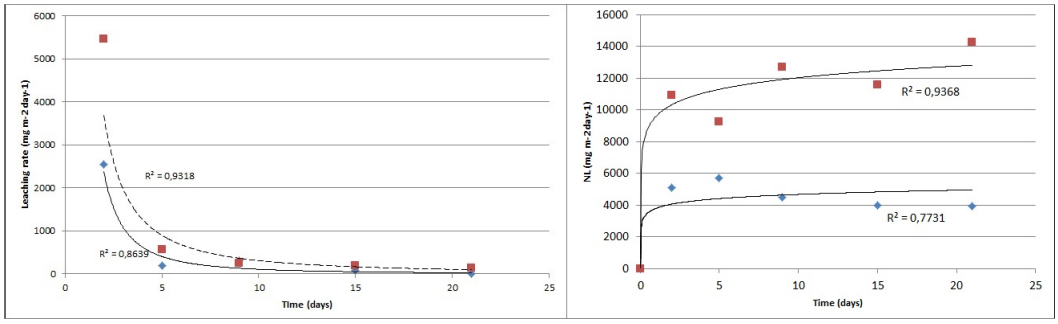

Figure 3.27: Leaching rates and normalized mass loss of strontium in solution measured for samples $Cs_{0.6}Sr_{0.4}[Zr_{1.6}Fe_{0.4}(PO_4)_3]$ in red and $Cs_{0.4}Sr_{0.3}[Zr_2(PO_4)_3]$ in blue.

For the first few days we see a gradual decrease in leaching this is due to the impurities of the pellet, this causes a heightened leaching rate after approximately 21 days the leaching rate becomes constant as it is limited by diffusion. The leaching rates after 21 days for $Cs_{0.6}Sr_{0.4}[Zr_{1.6}Fe_{0.4}(PO_4)_3]$ and $Cs_{0.4}Sr_{0.3}[Zr_2(PO_4)_3]$ are 131 $\frac{mg}{m^2 day}$ and 12.4 $\frac{mg}{m^2 day}$ respectively. These values are quite high which is to be expected as the use of the Soxhlet set-up constantly introduces fresh leachant rather than a static experiment where leaching rates were found to be lower at 5.9 $\frac{mg}{m^2 day}$ [20]. However these values might still decrease while approaching the equilibrium.
The found leaching rates show great promise for the possible immobilization of cesium and strontium, even though there is no solid solution cesium's leaching rate was too low to be measured and strontium's is acceptable.

3.1.6. Thermal analysis of the sample $Cs_{0.6}Sr_{0.4}[Zr_{1.6}Fe_{0.4}(PO_4)_3]$

The sample of composition $Cs_{0.6}Sr_{0.4}[Zr_{1.6}Fe_{0.4}(PO_4)_3]$ was chosen for the DTA/TG analysis because it models the waste stream compositions most accurately [4]. Simultaneous TGA and DTA measurements were done on the powder precursor of this sample prepared at 400 °C by the mechanochemical synthesis as shown in figure 3.28 using a heating rate of 10 °C per minute and an end temperature of 1500 °C.

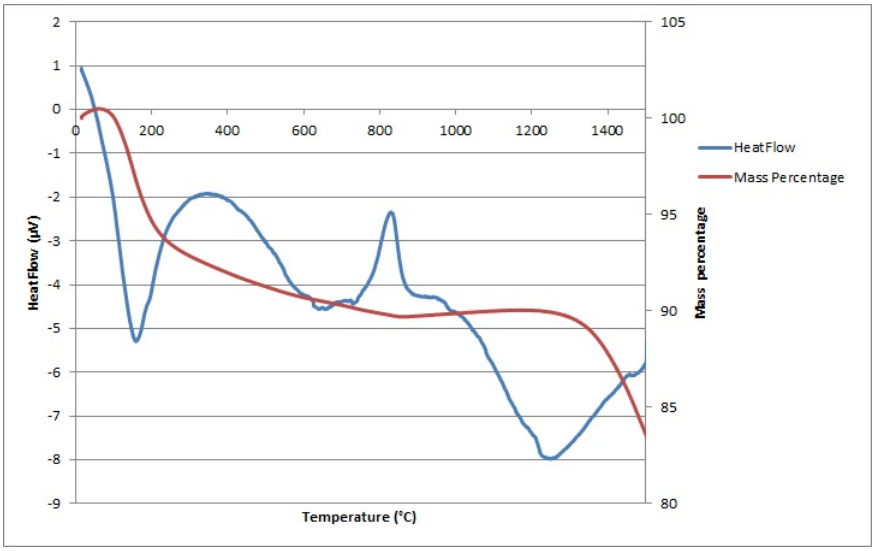

Figure 3.28: Simultaneous TGA and DTA measurements of the sample $Cs_{0.6}Sr_{0.4}[Zr_{1.6}Fe_{0.4}(PO_4)_3]$.

The first change is found around 100-200 °C here we observe a high decrease in mass and an endothermic peak, this is due to the evaporation of water trapped within the sample. Subsequently starting at approximately 750 °C we see a exothermic peak but little to no change in mass, meaning this is the temperature of crystallization. The crystallization has a maximum around 820 °C which explains the reduced crystallinity in samples synthesized at only 800 °C shown in 3.1.3. At increasing temperatures centered around 1300 °C we observe a broad endothermic peak and a high loss of mass afterwards indicating to the decomposition of the NZP phase, this temperature corresponds with the possible temperature of decomposition following the trend found by Pet'kov et al. [18].

3.2. Cerium containing NZP-type ceramics

3.2.1. Synthesis of $Ce_{0.25}[Zr_2(PO_4)_3]$

Tetravalent cerium in NZP,in the form of $Ce_{0.25}[Zr_2(PO_4)_3]$ was synthesized by the procedure described in section 2.1.2 with heating at 800 °C in air. Both the unheated precursor as well as the sample were characterized via X-ray diffraction and phase analysis were done as shown in figure 3.29.

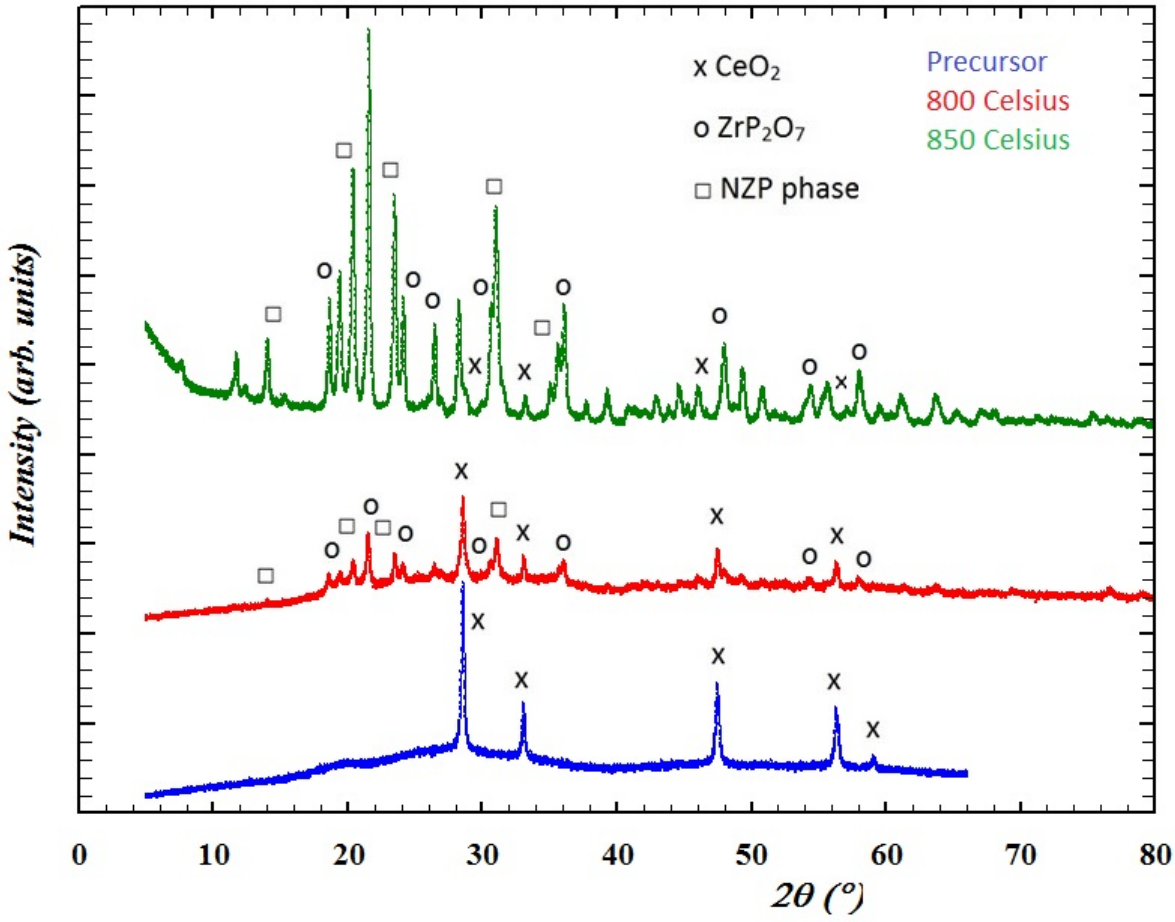

Figure 3.29: Phase analysis of the precursor powder and the sample with the composition $Ce_{0.25}[Zr_2(PO_4)_3]$ heated at 800 and 850 °C.

After heating of the sample at 800 °C we observe the presence of three phases: Cerium dioxide, Zirconium pyrophosphate, and a phase with the structure of NZP. The presence of cerium dioxide means not all of the powder has reacted, this is further proven by the substantial presence of zirconium pyrophosphate. This means that rather than form the NZP, $Ce_{0.25}[Zr_2(PO_4)_3]$, cerium remains unreacted as dioxide and zirconium forms the pyrophosphate as the by-product. All other powder intermediates remain in an amorphous phase as can be seen by the high background.
In order to promote further crystallization of these amorphous phases an additional heating step was carried out at 850 °C, this sample was also characterized via X-ray diffraction and phase analysis were done as can be seen in figure 3.29,.
As shown by figure 3.29 the amount of amorphous components and cerium dioxide was reduced significantly shown by the reduction in background and cerium dioxide peak intensity. Subsequently the intensity of the NZP phase peaks has improved, however this is even more so the case for zirconium pyrophosphate as those peaks have greatly increased in intensity. So it seems that whilst this additional heating brought further crystallization to both phases, it preferred zirconium pyrophosphate which has

become the dominant phase. This indicates that pyrophosphate forms as a by-product and remains in the mixture, the heating does not decompose it but rather promotes its further crystallization. In order to calculate the cell parameters a profile fit was done with the present phases: cerium dioxide, zirconium pyrophosphate and NZP, shown in figure 3.30.

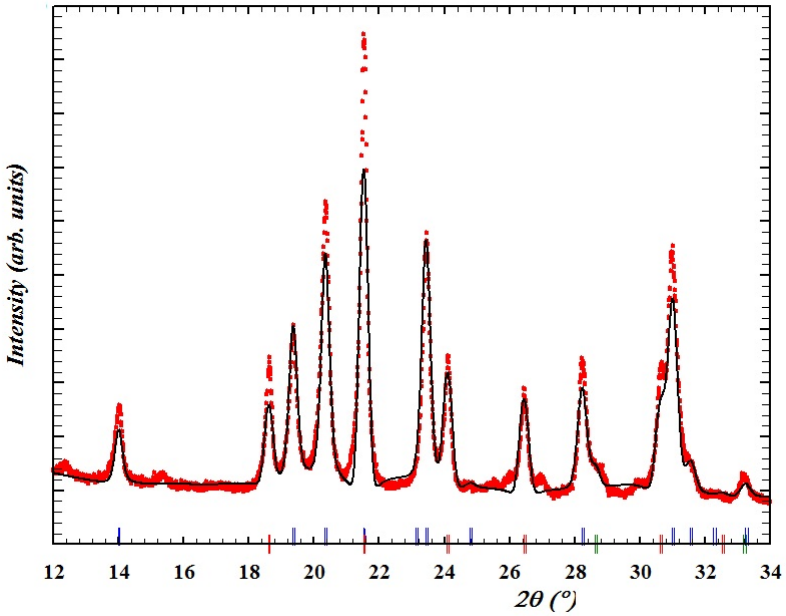

Figure 3.30: Part of the full profile fit on the sample $Ce_{0.25}[Zr_2(PO_4)_3]$. The experimental data is shown in red, theoretical curve in black and the difference in blue

The cell parameters for the NZP phase were found to be 8.726 $\pm$ 0.004 Å for the a-parameter and 23.06 $\pm$ 0.02 Å for the c-parameter. These values show a decrease compared to the cell parameters calculated by Bykov et al. [16] for $Ce_{0.33}[Zr_2(PO_4)_3]$ which were found to be 8.7419 Å for a and 23.128 Å for c. This gives the indication that $Ce_{0.25}[Zr_2(PO_4)_3]$ was successfully synthesized as Ce^{4+} is both a smaller cation and would fill fewer M1 positions leading to the observed decrease of cell parameters.

3.2.2. Synthesis of $Ce_{0.33}[Zr_2(PO_4)_3]$

An attempt was made to synthesize trivalent cerium in NZP, in the form of $Ce_{0.33}[Zr_2(PO_4)_3]$. To this end the procedure was followed as described in section 2.1.2 but heating at 600 °C was done in argon atmosphere. However when analysed with Powdercell, as shown in figure 3.31, we find that the formed NZP phase is in fact not $Ce_{0.33}[Zr_2(PO_4)_3]$ but likely $Ce_{0.25}[Zr_2(PO_4)_3]$ instead.

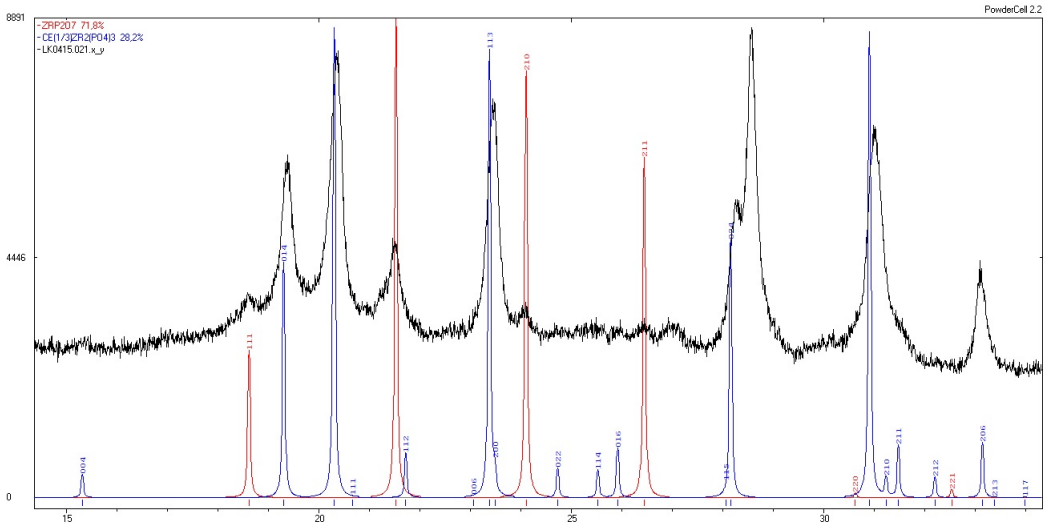

Figure 3.31: Phase analysis performed using Powdercell on the sample $Ce_{0.33}[Zr_2(PO_4)_3]$. Experimental diffraction pattern is shown in black, and theoretical bragg peaks of $Ce_{0.33}[Zr_2(PO_4)_3]$ and zirconium pyrophosphate in blue and red respectively.

The presence of zirconium pyrophosphate in this sample can be used as an internal standard, as shown in the figure only the NZP peaks shift meaning we are not dealing with an instrumental shift. Which means that likely the cerium did not reduce and we have $Ce_{0.25}[Zr_2(PO_4)_3]$ rather than $Ce_{0.33}[Zr_2(PO_4)_3]$. This is proven when this sample is compared to the earlier sample of $Ce_{0.25}[Zr_2(PO_4)_3]$ as can be seen in figure 3.32.

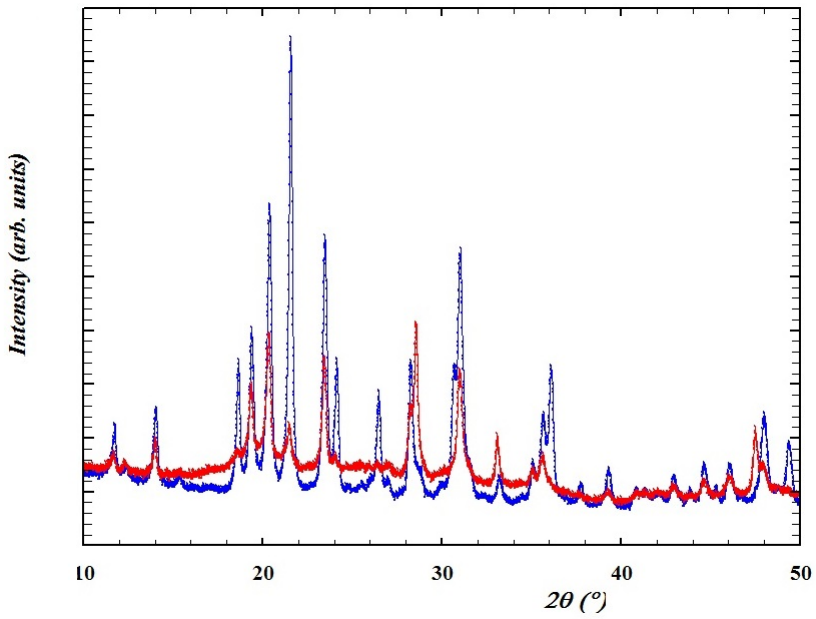

Figure 3.32: Powder diffraction patterns of two samples, $Ce_{0.25}[Zr_2(PO_4)_3]$ one heated at 600 °C in argon atmosphere, in red, and the other heated at 800 and 850 °C in air, in blue.

To calculate the cell parameters of the NZP phase the same procedure was used as described in section 3.2.1. The resulting cell parameters were 8.729 $\pm$ 0.009 Å for a and 23.05 $\pm$ 0.04 Å for c. These values are very similar to the ones found in section 3.2.1 proving that this synthesis route did not reduce cerium and instead formed $Ce_{0.25}[Zr_2(PO_4)_3]$.
We found that it is possible to synthesize crystalline NZP starting from tetravalent cerium in the form of cerium dioxide in the M1 position, this method could therefor be used to form such NZP type ceramics using uranium or thorium dioxide.

4

Conclusion

NZP type ceramics containing cesium and strontium were successfully synthesized using the mechanochemical synthesis method, however the formation of solid solutions was limited to the series of $Sr_{1-(x/2)}[Zr_{1+x}Fe_{1-x}(PO_4)_3]$. To this end the pechini method of synthesis was tried on the sample with composition $Cs_{0.6}Sr_{0.4}[Zr_{1.6}Fe_{0.4}(PO_4)_3]$ however this did not promote the formation of a solid solution.

Cell parameter calculations were done on each sample resulting in a linear relationship in accordance with Vegard's law for the solid solution $Sr_{1-(x/2)}[Zr_{1+x}Fe_{1-x}(PO_4)_3]$ whilst the other series showed irregular change in cell parameters.

IR spectra of these cesium and strontium containing NZP type ceramics were measured proving the space group for the end members $Sr_{0.5}[Zr_2(PO_4)_3]$, $Cs[Zr_2(PO_4)_3]$ and $Sr[ZrFe(PO_4)_3]$. All of the samples were found to belong to the orthophosphate class proving the NZP structure.

Leaching rates of strontium in samples of composition $Cs_{0.6}Sr_{0.4}[Zr_{1.6}Fe_{0.4}(PO_4)_3]$ and $Cs_{0.4}Sr_{0.3}[Zr_2(PO_4)_3]$ were determined to be 131 $\frac{\mathrm{mg}}{\mathrm{m^2 day}}$ and 12.4 $\frac{\mathrm{mg}}{\mathrm{mg^2 day}}$ respectively after Soxhlet leaching of 21 days, leaching rates for the other cations were unable to be accurately determined.

Thermal analysis was done on the sample with composition $Cs_{0.6}Sr_{0.4}[Zr_{1.6}Fe_{0.4}(PO_4)_3]$ which proved the temperature of crystallization at around 800 °C whilst the decomposition temperature was found to be approximately 1300 °C.

Trivalent cerium containing NZP type ceramics were not successfully synthesized however the synthesis of NZP containing tetravalent cerium was successful albeit with low crystallinity.

A

Acknowledgements

I would like to thank the research group of NERA for giving me the possiblity to do my bachelor's thesis there, and Denis Bykov for being my supervisor along this project. Furthermore I would like to thank Astrid van de Meer and Baukje Terpstra of RIH and Peter van der Baan en Dick de Haas of NERA for helping me with my experiments. Lastly I would like to thank Kees Goubitz for his help with the XRD and Hans Brouwer for the assistance with the DTA/TG experiment.

B

Future Work

In future work the effect of irradiation on the structure and macroscopic properties of the NZP type ceramics could be investigated. Additionally more accurate thermal analysis should be done of these NZP type ceramics to further determine the exact temperatures of crystallization and decomposition. The formation of cesium and strontium containing solid solutions should be further studied using different methods of synthesis. And lastly the synthesis of tetravalent cerium in NZP should be further optimized to find higher crystallinity before the procedure can be tested using uranium or thorium dioxide.

Bibliography

[1] W. N. Association, *Safety of nuclear power reactors,* (2015), [Online; accessed 29-June-2015].

[2] W. N. Association, *Radioactive waste management,* (2015), [Online; accessed 9-March-2015].

[3] N. Colonna, F. Belloni, E. Berthoumieux, M. Calviani, C. Domingo-Pardo, C. Guerrero, D. Karadimos, C. Lederer, C. Massimi, C. Paradela, R. Plag, J. Praena, and R. Sarmento, *Advanced nuclear energy systems and the need of accurate nuclear data: The n-TOF project at CERN,* Energy and Environmental Science **3**, 1910 (2010).

[4] J. Law, T. Garn, R. Herbst, D. Meikrantz, and D. Peterman, *Development of cesium and strontium seperation and immobilization technologies in support of an advanced nuclear fuel cycle,* in *Waste management 2005* (Tuscon, AZ., 2006).

[5] I. Donald, B. Metcalfe, and R. Taylor, *The immobilization of high level radioactive wastes using ceramics and glasses,* Journal of Material Science **32**, 5851 (1997).

[6] J.-M. Montel, *Minerals and design of new waste forms for conditioning nuclear waste,* Comptes Rendus Geoscience **343**, 230 (2011).

[7] E. Vance, *Comprehensive Nuclear Materials Volume 5, Material Performance and Corrosion/Waste Materials,* (Elsevier, 2012) Chap. 5.19 Ceramic Waste Forms.

[8] H. Mimura, T. Hirabayashi, and M. Ozawa, *Leachability and Thermal Properties of Ceramic Solid Forms Immobilizing Cesium and/or Strontium,* in *Nuclear Energy for New Europe 2003* (Portoroz, Slovenia, 2003).

[9] R. Hazen, L. Finger, D. Agrawal, H. McKinstry, and A. Perrotta, *High-temperature crystal chemistry of sodium zirconium phosphate (NZP),* Journal of Materials Research **2**, 329 (1987).

[10] L.-O. Hagman and P. Kierkegaard, *The crystal structure of $NaMe^{IV}_2(PO_4)_3$; Me=Ge, Ti, Zr,* Acta chemica scandinavica **22**, 1822 (1968).

[11] A. I. Orlova, V. Y. Volgutov, G. R. Castro, S. García-Granda, S. A. Khainakov, and J. R. García, *Synthesis and crystal structure of NZP-type thorium-zirconium phosphate,* Inorganic chemistry **48**, 9046 (2009).

[12] K. Momma and F. Izumi, *VESTA 3 for three-dimensional visualization of crystal, volumetric and morphology data,* Journal of Applied Crystallography **44**, 1272 (2011).

[13] J. Alamo, *Chemistry and properties of solids with the [NZP] skeleton,* Solid State Ionics **63-65**, 547 (1993).

[14] H. T. Hawkins, D. R. Spearing, D. K. Veirs, J. A. Danis, D. M. Smith, C. D. Tait, W. H. Runde, M. N. Spilde, and B. E. Scheetz, *Synthesis and characterization of uranium(IV)-bearing members of the [NZP] structural family,* Chemistry of Materials **11**, 2851 (1999).

[15] A. Bohre and O. Shrivastava, *Crystallographic evaluation of sodium zirconium phosphate as a host structure for immobilization of cesium and strontium,* International Journal of Applied Ceramic Technology **10**, 552 (2013).

[16] D. M. Bykov, E. R. Gobechiya, Y. K. Kabalov, A. I. Orlova, and S. V. Tomilin, *Crystal structures of lanthanide and zirconium phosphates with general formula $Ln_{0.33}Zr_2(PO_4)_3$, where Ln=Ce, Eu, Yb,* Journal of Solid State Chemistry **179**, 3101 (2006).

[17] A. Orlova, *Isomorphism in Crystalline Phosphates of the $NaZr_2(PO_4)_3$ Structural Type and Radiochemical Problems, journal=Radiochemistry, year=2002, volume=44, pages=423-445,* .

[18] V. Pet'kov and E. Asabine, *Thermophysical properties of NZP ceramics (A review),* Glass and Ceramics **61**, 233 (2004).

[19] Goodfellow, *Borosilicate glass properties of borosilicate glass (pyrex duran) by goodfellow ceramic and glass division,* (2013), [Online; accessed 29-June-2015].

[20] A. Naik, S. Deb, A. Chalke, M. Saxena, K. Ramakumar, V. Venugopal, and S. Dharwadkar, *Microwave-assisted low temperature synthesis of sodium zirconium phosphate (NZP) and the leachability of some selected fission products incorporated in its structure - A case study of leachbility of cesium, year=2010, journal=Journal of chemical sciences, volume=122, pages=71-82„* .

[21] M. Sugantha and U. Varadaraju, *Synthesis and leachability studies of NZP and eulytine phases,* Waste management **18**, 275 (1998).

[22] M. L. Carter, A. L. Gillen, K. Olufson, and E. R. Vance, *HIPed tailored hollandite waste forms for the immobilization of radioactive Cs and Sr,* Journal of the American Ceramic Society **92**, 1112 (2009).

[23] P. Jagai, *Immobilization of Cs/Sr fraction of radioactive wastes into phosphorus containing compounds of NZP structure types*, Bachelor's thesis, TU Delft (2014).

[24] I. Gutzow and J. Schmelzer, *The Vitreous State: Thermodynamics, Structure Rheology, and Crystallization,* (Springer, 2013) Chap. 4.2 Goldschmidt's Rule.

[25] T. Rojac and M. Kosec, *Mechanochemical synthesis of complex ceramic oxides,* (Woodhead publishing limited, 2010) Chap. 6 High-Energy Ball Milling: Mechanochemical Processing of Nanopowders.

[26] H. Lee, M. Hong, S. Bae, H. Lee, E. Park, and K. Kim, *A novel approach to preparing nano-size Co_3O_4-coated Ni powder by the Pechini method for MCFC cathodes,* Journal of Materials chemistry **13**, 2626 (2003).

[27] M. Barre, M. Crosnier-Lopez, F. Le Berre, J. Emery, E. Suard, and J.-L. Fourquet, *Room Temperature Crystal Structure of $La_{1/3}Zr_2(PO_4)_3$, a NASICON-type compound,* Chemistry of Materials **17**, 6605 (2005).

[28] D. Bregireux, R. Belin, P. Valenza, F. Audubert, and D. Bernache-Assollant, *Plutonium and americium monazite materials: Solid state synthesis and X-ray diffraction study,* Journal of Nuclear Materials **366**, 52 (2007).

[29] R. Dinnebier and K. Friese, *Modern XRD Methodes in Mineralogy,* Max-Planck-Institute for Solid State Research.

[30] W. Kraus and G. Nolze, *POWDER CELL - a program for the representation and manipulation of crystal structures and calculation of the resulting X-ray Powder patterns,* Journal of Applied Crystallography **29**, 301 (1996).

[31] T. Degen, M. Sadki, E. Bron, U. König, and G. Nénert, *The HighScore suite,* Powder Diffraction **29**, S13 (2014).

[32] P. Villars and K. Cenzual, *Pearson's Crystal Data: Crystal structure Database for Inorganic Compounds, Release 2014/15,* ASM International®, Materials Park, Ohio, USA (2015).

[33] H. Rietveld, *A Profile Refinement Method for Nuclear and Magnetic Structures,* Journal of Applied Crystallography **2**, 65 (1969).

[34] L. McCusker, R. Von Dreele, D. Louër, and P. Scardi, *Rietveld Refinement Guidelines,* Journal of Applied Crystallography **32**, 36 (1999).

[35] J. Rodriguez-Carvajal, *FULLPROF: A Program for Rietveld Refinement and Pattern Matching Analysis,* Abstracts of the Satellite Meeting on Powder Diffraction of the XV Congress of the IUCr, p. 127, Toulouse, France (1990).

[36] A. Le Bail, *Whole powder pattern decomposition methods and applications: A retroscpection,* Powder Diffraction **20**, 316 (2005).

[37] L. Berzina-Cimdina and N. Borodajenko, *Research of Calcium Phosphates Using Fourier Transform Infrared Spectroscopy,* (Intech, 2012) Chap. 6 Infrared Spectroscopy - Materials Science, Engineering and Technology.

[38] E. Ordónez-Regil, C. Contreras-Ramirez, S. Fernández-Valverde, P. González-Martínez, and H. Carrasco-Ábrego, *Crystal Growth and Thermoluminescence Response of $NaZr_2(PO_4)_3$ at High Gamma Radiation Doses,* Journal of Nuclear Materials **443**, 417 (2013).

[39] A. Stefánsson, I. Gunnarsson, and N. Giroud, *New methods for the direct determination of dissolved inorganic, organic and total carbon in natural waters by Reagent-Free™ Ion Chromatography and inductively coupled plasma atomic emission spectrometry,* Analytica Chimica Acta **582**, 69 (2007).

[40] H. Bhadesia, *Thermal analyses techniques. Differential thermal analysis,* University of Cambridge, Material Science and Metallurgy.

[41] A. Coats and J. Redfern, *Thermogravimetric analysis. A review,* Analyst **88**, 906 (1963).

[42] A. Kryukova, *X-Ray diffraction studies of double phosphates in the sodium-zirconium-phosphate family,* Russian Journal of Inorganic Chemistry **36**, 1108 (1991).

[43] S. Bahl, T. Pruessmann, A. Kutzer, V. Koldeisz, T. Yokosawa, I. Pidchenko, G. Roth, H. Geckeis, and V. Vitova, *Impact of increasing MoO_3 loading on the composition of multicomponent borosilicate glass,* in *Actinide XAS 2014* (Schloss Böttstein, 2014).

[44] A. Denton and N. Ashcroft, *Vegard's law,* Physical Review A **43**, 3161 (1991).

[45] V. Pet'kov, E. Asabina, A. Markin, and N. Smirnova, *1. Synthesis, Characterization and Thermodynamic Data of Compounds with NZP structure,* Journal of Thermal Analysis and Calorimetry **1147**, 35 (2008).

[46] V. Kurazhkovskaya, A. Orlova, V. Pet'kov, D. Kemenov, and L. Kaplunnik, *IR study of the structure of rhombohedral zirconium and alkali metal orthophopshates,* Journal of structural chemistry **41**, 61 (2000).

[47] A. Bohre and O. Shrivastava, *Crystal chemistry of immobilization of divalent Sr in ceramic matrix of sodium zirconium phosphates,* Journal of Nuclear Materials **433**, 486 (2013).

[48] M. Sugantha and U. Varadaraju, *Synthesis and Characterization of NZP phases, $AM'^{3+}M''^{4+}P_3O_{12}$,* Journal of solid state chemistry **111**, 33 (1994).

[49] E. Borovikova, V. Kurazhslovskaya, D. Bykov, and A. Orlova, *Infrared Spectroscopy and the Structure of $La_{0.33}Zr_2(PO_4)_3$-$Yb_{0.33}Zr_2(PO_4)_3$ Solid solutions,* Journal of Structural Chemistry **51**, 40 (2010).